JGR Earth Surface

Key Points:

- Coupled fluid-solid simulations of geophysical flows against flexible, slit and rigid barriers reveal their distinct intercepting mechanisms
- The flexible barrier performs the best under runup mode owing to its high permeability and Fr-dependent load-deflection behavior
- Compilation of a barrier-specific design diagram highlights the effects of large particles, barrier permeability, and structure deformability

How Flexible, Slit and Rigid Barriers Mitigate Two-Phase Geophysical Mass Flows: A Numerical Appraisal

Yong Kong[1] , Mingfu Guan[1] , Xingyue Li[2] , Jidong Zhao[3] , and Haochen Yan[1]

[1]Department of Civil Engineering, The University of Hong Kong, Hong Kong, China, [2]Department of Geotechnical Engineering, College of Civil Engineering, Tongji University, Shanghai, China, [3]Department of Civil and Environmental Engineering, The Hong Kong University of Science and Technology, Hong Kong, China

Abstract Flexible, slit, and rigid barriers are common countermeasures to mitigate natural geophysical mass flows, but presently, quantitative comparisons of their performance are lacking, due to the challenges involved in accurately representing the multi-body and multi-phase interactions. This study presents a numerical appraisal on this issue using a physics-based coupled computational fluid dynamics and discrete element method (CFD-DEM). A geophysical flow is considered as a mixture of discrete gap-graded particles (DEM) and a continuous viscous slurry (CFD), whereas a permeable and deformable barrier structure can be modeled by DEM. The in-flow multiphase interactions and flow-barrier interactions can be rigorously modeled by a coupling scheme between DEM and CFD. Our numerical simulations reasonably capture both field and experimental observations on key features of flow-barrier interactions and barrier responses. The different intercepting mechanisms of three barriers via pile-up and runup modes are revealed by qualitative and quantitative characterizations. Flexible barriers perform the best under runup mode regarding much larger peak load reduction ratios (up to 89%) due to their high permeability and *Fr*-dependent load-deflection behavior. We further compile a barrier-specific design diagram that suggests existing analytical models calibrated by limited experiments may underestimate the peak impact for slit and rigid barriers due to their neglect of large solid particles in the impinging flows while leading to overestimations for flexible barriers owing to inappropriate representations of barrier permeability and structural deformability. Our findings may offer a basis for model improvements and developments in practical barrier selection and design.

Plain Language Summary Engineers commonly use flexible, open-type, and closed-type barriers to reduce the adverse impacts of natural geophysical mass flows. However, the selection and design of barriers mainly rely on engineering experience and simplified models. We present a numerical study based on the coupled fluid-solid modeling to offer quantitative reference on this issue. The numerical framework employed enables a unified description of a geophysical flow as a mixture of solid particles and a continuous viscous slurry and any of the three barrier types, offering a consistent comparison basis. We compare the different intercepting mechanisms of three types of barriers in resisting an impinging flow and identify their intertwined dependence of incoming flow characteristics, barrier deformability and passing ability, and peak impact loads. A flexible barrier is found to outperform the other two in achieving better peak load reduction ratios (up to 89%) with a runup mode, due to its high passing ability and load-deflection behavior. The compilation of a unified barrier-specific design diagram highlights the influences of barrier passing ability, structure deformability, and large solid particles on the peak impacts. This work could help for developing better analytical models on specific barrier design to mitigate natural geohazards caused by geophysical mass flows.

1. Introduction

The ever-growing climate change, extreme weather events, and continuous expansion of human populations into mountainous regions have contributed to the increase in the frequency, intensity, and duration of catastrophic geophysical mass flows (Fowler et al., 2021; Guerreiro et al., 2018; Hirschberg et al., 2021), such as debris flows, lahars and avalanches. In practical combats of these flows, flexible, slit, and rigid barriers (see Figure S1 in Supporting Information S1) are designed to reduce their peak discharge, flow velocity, erosion, and run-out distance (Gong et al., 2021; Iverson et al., 2016; Marchi et al., 2019). Nonetheless, current practice on the selection of barrier types and associated design has been largely empirical, since there is no unified analytical tool available for systematic analysis and comparison of their performance in arresting impinging flows of variable nature. This is due to the difficulties posed by the modeling of multi-body and multi-phase interactions. For

Writing – review & editing: Yong Kong, Mingfu Guan, Xingyue Li, Jidong Zhao, Haochen Yan

instance, a two-phase geophysical flow against a flexible barrier involves spatial-temporal force distributions and transmissions, systematic structure responses, and difficult-to-estimate energy dissipations and conversions, making it difficult for the field, experimental and numerical analysis and thus remain poorly understood. In addition, probing such intricate interactions of perplexing physics is important in many natural and industrial processes, including stent-induced hemodynamics (Gori et al., 2019; Jiménez & Davies, 2009), ocean engineering with rigid and deformable structures (Amini et al., 2008; Sun et al., 2021), as well as the mitigation of geophysical mass flows (Ng et al., 2017; Song, Zhou, et al., 2021).

Fundamentally, the overall impact processes of geophysical flows impacting flexible, slit, and rigid barriers are predominantly governed by two modes: pile-up (momentum jump reflected upstream) and runup (high energy jet deflected vertically) (e.g., Kong, Li, & Zhao, 2021; Song, Choi, Ng, & Zhou, 2018; Song et al., 2017; Vicari et al., 2021), as illustrated in Figure 1. When a geophysical flow first impacts a flexible, slit or rigid obstacle, a slow flow produces a gentle pile-up of the jammed debris upstream of the barrier (Figures 1a1, 1b1 and 1c1), whilst a faster flow gives rise to a runup or vertical jet impact (Figures 1a3, 1b3 and 1c3). Eventually, a gentle overflow occurs under pile-up mode (Figures 1a2, 1b2 and 1c2), while a large jet or fast overspreading forms downstream of a barrier under runup mode (Figures 1a4, 1b4 and 1c4). The size (Faug, 2015) and shape (trapezoid or triangle; Kong, Li, & Zhao, 2021) of the dead zone formed upstream of a barrier serve as good indicators to distinguish the prevailing impact modes. Faug (2015) reported that both the Froude number (Fr) of the incoming flow and the barrier-flow height ratio strongly affect the dead zone (formation, shape, and size) and prevailing impact regimes for granular-wall interactions. Note that Fr is universally used to characterize impinging flow dynamics (Faug, 2015, 2021), which is defined as $Fr = v_0 / \sqrt{gh_0 \cos\theta}$ with gravitational acceleration g. Relative to the rigid barrier, partial materials of impinging flows can pass through flexible and slit barriers (Figures 1a and 1b). In particular, a flexible barrier can significantly deform to attenuate flow impacts and extend interaction duration (Figure 1a). Moreover, differentiating the predominated impact mode serves as a critical theoretical basis for the adoption of various analytical models and empirical coefficients in countermeasure designs (Kong, Li, & Zhao, 2021; Wendeler et al., 2019). The individual contribution of the solid and the fluid in flows on the impact load remains unclear, especially during impact mode transitions for different barriers. Although the two impact modes for different barriers in arresting geophysical flows have been discussed individually with phenomenological closures and idealized assumptions (Ashwood & Hungr, 2016; Liu et al., 2020), a unified picture revealing the differing mechanisms via two impact modes for three types of barriers with both qualitative and quantitative characterizations remains elusive.

Models to predict the peak impact load and maximum runup height are essential for barrier designs. Popular analytical models established for predicting the peak impact include the hydro-static models (Armanini, 1997; Lichtenhan, 1973), the hydrodynamic models (Hungr et al., 1984; Scheidl et al., 2013), and the mixed or hybrid models (Arattano & Franzi, 2003; Li et al., 2021). Estimations of the peak impact and maximum runup height in conjunction with the Froude number (Fr) require theoretical functions and empirical relations, which have been investigated in extensive studies (Ng et al., 2017; P. Cui et al., 2015; Song, Zhou, et al., 2021; Vagnon, 2020). The Fr-related models, coefficients, and relations are widely adopted in designing various flow-resisting countermeasures, including flexible, slit, and rigid barriers (Hu et al., 2020; Kwan & Cheung, 2012; Wendeler, 2016). Nonetheless, their results vary substantially due to the following limitations. (a) Current models are obtained based on either energy or mass and momentum conservations with idealized presumptions, such as jump length $L = 0$, the density ratio $\rho_1/\rho_0 = 1$, no energy dissipation, and no mass and momentum loss. In reality, the jump (Figures 1a1, 1b1 and 1c1) is typically highlighted with a smooth transition with a reverse "S" shaped profile (Faug, 2015), and ρ_1/ρ_0 across the jump substantially deviates from unity owing to the changing solid fraction (Albaba et al., 2018; Pudasaini & Mergili, 2019). (b) Their values depend on the specific impinging flow properties, barrier types, and geometries. For instance, empirical coefficients and relations are mainly calibrated by limited tests without considering large particles in mixture flows (Armanini et al., 2020; Song, Chen, et al., 2021), which significantly differs from natural occurred geophysical flows. (c) Current models used for flexible barrier designs commonly ignore the combined effects of barrier permeability and structure deformability, introducing a remarkable overestimation of the peak impact load (Song, Zhou, et al., 2021; Tan et al., 2019). Therefore, systematic tests with two-phase geophysical flows carrying large particles against flexible, slit, and rigid barriers are warranted to quantify the influences of Fr, barrier permeability, and structure deformability on the peak impact and maximum runup height, and thus to offer a potential improvement on analytical models and engineering designs for various flow-resisting barriers.
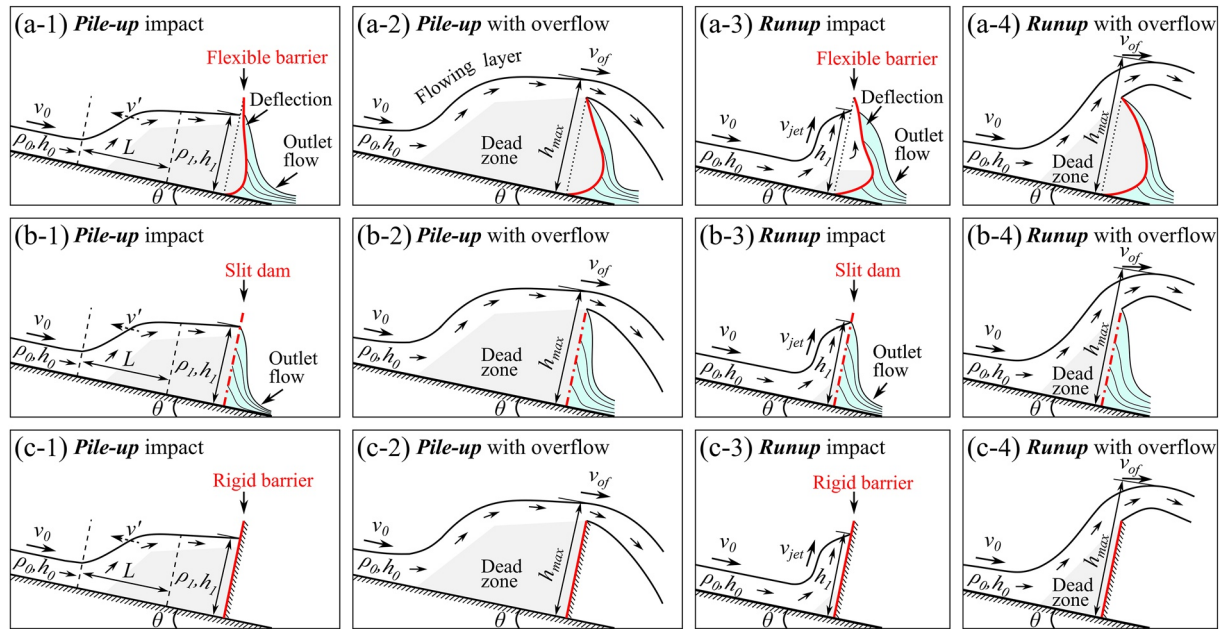
Figure 1. Schematic illustrations of alternative impact modes in geophysical flows impacting (a) flexible, (b) slit, and (c) rigid barriers: pile-up and runup modes (v_0, ρ_0, and h_0, the pre-impact velocity, bulk density, and flow thickness of impinging flows, respectively; L, ρ_1 and h_1, jump length, downstream density, and the pile-up height or runup height, respectively; v', v_{jet}, and v_{of}, the velocities of moving jump interface, vertical jet, and overflow, respectively; h_{max} and θ, the maximum runup height and slope angle, respectively).

Compared with slit and rigid countermeasures (Zhou, Du, et al., 2020; Iverson et al., 2016), flexible barriers are economical and easy to install and replace in mountainous regions. Consequently, they are increasingly used to protect critical infrastructures and residential areas from debris flows, snow avalanches, and rock avalanches (Bugnion et al., 2012; Wendeler, 2016). Abundant studies have investigated the interactions between geophysical flows and flexible barriers. Both the full-scale and large-scale tests offer valuable data but are relatively expensive (Brighenti et al., 2013; DeNatale et al., 1999; Tan et al., 2019; Vicari et al., 2021). Although the small-scale experiments enable systematic investigations under well-controlled conditions, they commonly use simplified flexible barriers, such as impermeable membranes (Ashwood & Hungr, 2016; Song, Zhou, et al., 2021) and uniform plastic meshes (Wendeler et al., 2019), which may fail to recover the barrier permeability and nonuniformity. Moreover, the crucial load-deflection behavior of a flexible barrier is currently hampered by the difficult-to-estimate spatial-temporal loads and deformations. Alternatively, numerical methods serve as a rational way to explore this issue that includes continuous methods (finite element method [FEM], Lambert et al., 2021; L. Zhao et al., 2020; Material Point Method, Ng et al., 2020), discrete methods (discrete element method [DEM], Albaba et al., 2017; Zhu et al., 2019; smoothed particle hydrodynamics [SPH], Fávero Neto et al., 2020), and the coupled frameworks (FEM-DEM, Liu et al., 2020; SPH-DEM, Wu et al., 2018; Lattice Boltzmann Method coupled with DEM and FEM, Leonardi et al., 2016; FEM-computational fluid dynamics [CFD], Von Boetticher et al., 2011; CFD-DEM, Kong, Li, & Zhao, 2021). However, current studies (Kong, Li, & Zhao, 2021; Liu et al., 2020; L. Zhao et al., 2020) commonly generate the barrier net units in a 2D plane by ignoring their frictional sliding in the 3D space, resulting in unrealistic load sharing and transferring. A flexible ring net barrier (Figures 1a and 3b) typically consists of the main ring net, cables, and energy dissipators, which have been rarely captured in a unified method. On the other hand, the solid-liquid nature of a two-phase geophysical flow plays a crucial role in predicting erosion, impact and deposition features (Breard et al., 2020; Zhou, Cui, et al., 2020; K. F. Cui et al., 2021). Nonetheless, the flow-barrier interactions have commonly been simulated by continuum flows or dry flows (Ng et al., 2020; Von Boetticher et al., 2011; Zhu et al., 2019). Therefore, a physically based numerical model is exigently needed to capture these actual situations, such as the cable-ring-ring sliding and the multi-phase interactions.

Herein a unified CFD-DEM method is employed to model the complex interactions during a two-phase geophysical flow impacting flexible, slit and rigid barriers. Based on systematic tests, qualitative and quantitative analysis are performed particularly from the following perspectives:

1. Analyze the different intercepting mechanisms via pile-up and runup modes by qualitative descriptions of the key flow-barrier interactions and temporal quantifications on the individual contribution of the fluid and the solid in flows on the impact load;
2. Quantify the peak load reduction and elongated impact duration ratios for both flexible and slit barriers relative to a rigid barrier, as well as the load-deflection relations for a flexible barrier; and
3. Present a unified design diagram comprising a barrier-specific data set from analytical models, experimental tests, field events, and our numerical results to reveal the influences of Fr, barrier permeability, and structure deformability on the peak impacts and normalized maximum runup heights.

2. Methods and Model Setup

A unified coupled CFD-DEM method is used in the study. It resolves the mixture nature of a two-phase geophysical mass flow by treating the solid particle and viscous fluid systems with DEM and CFD, respectively. Meanwhile, a flexible ring net barrier is simulated with DEM, by which its interaction with the solid and fluid phases in flows can be handily captured within the unified CFD-DEM framework. Note that both slit and rigid countermeasures are modeled as solid boundaries. The employed method solves the solid-fluid interactions by exchanging interaction forces and other information between DEM and CFD modules. It is capable of capturing the complicated fluid-solid interactions in classic geomechanics problems (J. Zhao & Shan, 2013; Li & Zhao, 2018) and various engineering conditions including flow-barrier interactions (Kong, Zhao, & Li, 2021; Li et al., 2021). Recently, this method has been extended to examine the impacts of debris flow on flexible barriers (Kong, Li, & Zhao, 2021; Li et al., 2020), where the modeling of different barrier components has been elaborated, calibrated, and verified. In what follows, we will briefly recall the key ingredients of the employed approach for modeling two-phase geophysical mass flows, flexible ring net barriers, and their interactions.

2.1. Modeling Two-Phase Geophysical Mass Flow

The modeling of two-phase geophysical mass flow is developed and validated in previous work (J. Zhao & Shan, 2013; Kong, Li, & Zhao, 2021; Li & Zhao, 2018; Li et al., 2020, 2021). For convenience, the model is also summarized here. The solid system of a geophysical mass flow is modeled by DEM. The translational and rotational motions of each particle i are governed by the following Newton's equations:

$$m_i \frac{d\mathbf{U}_i^p}{dt} = \sum_{j=1}^{n_i^c} \mathbf{F}_{ij}^c + \mathbf{F}_i^f + \mathbf{F}_i^g \qquad (1)$$

$$I_i \frac{d\omega_i}{dt} = \sum_{j=1}^{n_i^c} (\mathbf{M}_{t,ij} + \mathbf{M}_{r,ij}) \qquad (2)$$

where m_i and I_i are the mass and momentum of inertia of particle i, respectively. $\mathbf{U}_i^p$ and ω_i denote the translational and angular velocities of particle i, respectively. n_i^c is the total number of contacts for particle i. $\mathbf{F}_{ij}^c$, $\mathbf{M}_{t,ij}$, and $\mathbf{M}_{r,ij}$ are the contact force, tangential torque and rolling torque imposed on particle i from particle j or the walls, respectively. $\mathbf{F}_i^g$ is the gravitational force acting on the particle i. $\mathbf{F}_i^f$ is the fluid-particle interaction force acting on the particle i.

The fluid system (air and viscous liquid composed of water and fine-solid materials) in a geophysical mass flow is simulated by discretized fluid cells with the volume of fluid (VOF) method in CFD. The following continuity equation and locally averaged Navier-Stokes equation are solved for each fluid cell:

$$\frac{\partial(\varepsilon_f \rho_f)}{\partial t} + \nabla \cdot (\varepsilon_f \rho_f \mathbf{U}^f) = 0 \qquad (3)$$

$$\frac{\partial \left(\varepsilon_f \rho_f \mathbf{U}_f \right)}{\partial t} + \nabla \cdot \left(\varepsilon_f \rho_f \mathbf{U}^f \mathbf{U}^f \right) = -\nabla p - \mathbf{f}^p + \varepsilon_f \nabla \cdot \tau + \varepsilon_f \rho_f \mathbf{g} + \mathbf{f}^s \tag{4}$$

where $\mathbf{U}^f$ and p are the averaged velocity and pressure for fluid phase in a cell, respectively. $\mathbf{g}$ is the body force vector. $\varepsilon_f = v_{void}/v_c$ denotes the void fraction (i.e., porosity). v_{void} is the total volume of void in a cell that may contain either air or fluid or both. v_c is the cell volume. $\mathbf{f}^p$ is the interaction force acting on the fluid in a cell imposed by particle(s) inside the cell. $\mathbf{f}^s$ denote the surface tension force. The governing equations for the fluid phase are solved by the Finite Volume Method. The air-liquid interface is determined algebraically from phase fractions, and the phase fraction distribution is smeared over a few fluid cells with the VOF method. Note that the single-phase mixture VOF method saves computational costs compared to the more sophisticated drag-force-based multiphase models (Von Boetticher et al., 2016).

The three-dimensional expressions of stress tensor τ for Newtonian and non-Newtonian fluids are reduced to the following functions. The following constitutive equation is assumed to govern a Newtonian fluid:

$$\tau = \mu_f \dot{\gamma} \tag{5}$$

where τ, μ_f, and $\dot{\gamma}$ are the shear stress, viscosity, shear rate of the fluid, respectively. In this work, the air is simulated as a Newtonian fluid. Compared to water as the fluid phase (Li et al., 2020; Shan & Zhao, 2014), the viscous-plastic slurry in typical geophysical flows is treated as a more complicated non-Newtonian fluid modeled with the Herschel-Bulkley model (Huang & Garcia, 1998):

$$\tau = \tau_0 + \kappa \dot{\gamma}^n \tag{6}$$

where τ_0 and κ are the yield stress and consistency index of the fluid, respectively. n is the flow index of the fluid. $n > 1$ gives a shear-thickening fluid while $n < 1$ corresponds to a shear-thinning fluid. $n = 1$ leads to a Bingham fluid. Slurry and mudflow normally have a flow index smaller than 1 (Huang & Garcia, 1998; Remaître et al., 2005).

The fluid-solid interactions are considered by exchanging interaction forces $\mathbf{F}^f$ in Equation 1 between the CFD and DEM computations. Four interaction forces are considered, including drag force $\mathbf{F}^d$, buoyancy force $\mathbf{F}^b$, viscous force $\mathbf{F}^v$, and virtual mass force $\mathbf{F}^{vm}$ (J. Zhao & Shan, 2013; Z. Y. Zhou et al., 2010):

$$\mathbf{F}^f = \mathbf{F}^d + \mathbf{F}^b + \mathbf{F}^v + \mathbf{F}^{vm} \tag{7}$$

Details of these fluid-solid interaction forces have been presented in Text S2 in Supporting Information S1 and can be referred to literature (Di Felice, 1994; J. Zhao & Shan, 2013; Z. Y. Zhou et al., 2010).

A sequential iterative procedure is followed for the two-way coupling procedures between DEM and CFD computations. At each time step, the DEM first provides such information as the velocities and positions of particles. The positions of all particles are then matched with the fluid cells to calculate relevant information (e.g., porosity and assembled momentum source term $\mathbf{f}^p = 1/v_c \sum_{i=1}^{n_c} \mathbf{F}_i^f$) of each cell. When all state variables (e.g., averaged velocity and pressure) for each fluid cell are resolved by the CFD, the particle-fluid interaction forces acting on the centroid of each particle are updated and transferred back to the DEM to solve the particle system for the next time step. Detailed solution procedures can be found in J. Zhao and Shan (2013).

2.2. Modeling Flexible Ring Net Barrier System

Figure 2a shows the DEM model of the flexible ring net barrier composed of a ring net consisting of 382 interlocking rings, 5 supporting cables, and 10 brake elements. Its configurations are generally consistent with the trapezoidal-shaped flexible ring net barrier in New Zealand (Figure 2b). The field barrier is fixed on three sides (left, bottom, and right) by anchors and nails. Cables are designed to sustain the load transferred from the ring net and to transform the load to anchored boundaries (Figures 2a and 2b). The bottom cable and lateral edges of both the top and middle cables in the DEM model (Figure 2a) are fixed to mimic the anchored boundaries in the field (Figure 2b). Both ends of a horizontal supporting cable are equipped with two brake elements (Figures 2a and 2b), which are designed to lengthen significantly under debris flow impact loads. Consequently, the lengthened cable can better carry the orthogonal loads than the straight spanned one. In particular, Figure 2c
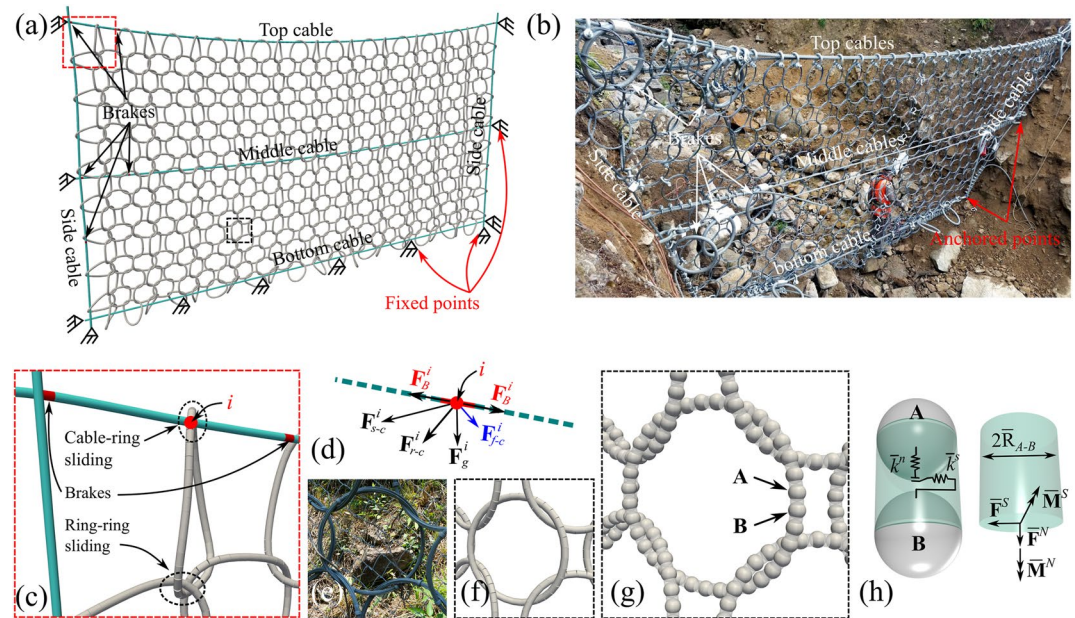
Figure 2. Discrete element method (DEM) model of a flexible ring net barrier. Comparison between (a) a reduced-scale flexible ring net barrier (by DEM) and (b) a full-scale ring net flexible barrier in New Zealand (Source: GEOVERT, 2016). (c) A zoom window shows the connections among interlocking ring elements, supporting cables, and brake elements. (d) Typical forces acting on a nodal particle i in the cable. Comparison of interlocking ring elements between (e) field photo and (f) DEM model. (h) Illustrates a parallel bond and the key parameters (see Text S3 in Supporting Information S1) adopted to describe the remote interaction between particles A and B in panel (g).

demonstrates an enlarged view of the area marked by a red dashed rectangular in Figure 2a. It shows the connections among the interlocking ring elements, cables, and brake elements where the cable-ring-ring frictional slidings are enabled. Moreover, the numerical reconstruction of the flexible barrier is introduced as follows. (a) Each ring is generated at their designed physical nodes in the 3D space and then rotated to avoid contact with the other rings. (b) Bonds are created between only adjacent particles within each ring. (c) Cables and energy dissipators are generated according to the barrier designs. (d) The whole flexible barrier is then pulled tautly.

Figure 2d illustrates the typical forces acting on the nodal particle i in a barrier cable, which consist of gravity force $\mathbf{F}_g^i$, the solid-cable contact force $\mathbf{F}_{s-c}^i$, the fluid-cable interaction force $\mathbf{F}_{f-c}^i$, the ring-cable contact force $\mathbf{F}_{r-c}^i$, and the bond force in the cable $\mathbf{F}_B^i$. Thus, the interaction between barrier particles and the fluid in flows can be considered in the same manner as the fluid-solid interactions in impinging flows, whereas the interaction between barrier particles and particles in flows can be naturally executed under the same umbrella of DEM. Consequently, the multi-body and multi-phase interactions during a two-phase geophysical flow against a flexible ring net barrier can be conveniently captured in a unified manner within the coupled CFD-DEM framework.

All the barrier components are modeled with DEM by using nodal particles connected with parallel bonds (Li et al., 2020; Potyondy & Cundall, 2004). The interlocking connections in a ring net can be realistically captured (Figures 2e and 2f). A real ring element (Figure 2e) consisting of a certain number of windings is idealized into a numerical mesh (Figure 2f) with a set of particles placed at the physical nodes of the ring (Figure 2g). All particles in a ring element are assumed to be identical in size. Figure 2h shows the parallel bond linking the nodal particles A and B within a ring element in Figure 2g. Specifically, this parallel bond can sustain the axial and shear-directed forces and moments, which are denoted by $\overline{\mathbf{F}}^n$, $\overline{\mathbf{F}}^s$ and $\overline{\mathbf{M}}^n$, $\overline{\mathbf{M}}^s$, respectively. Interested readers can refer to Text S3 in Supporting Information S1 and the literature (Li et al., 2020) for detail.

Analogously, a cable is modeled with a set of connected particles whose centers are along the cable (Figure 2c). A brake element is modeled with two particles connected by a parallel bond (Figure 2c). Different types of parallel bonds can be handily adopted to capture various behaviors of the barrier components. Assuming elastic response and constant stiffness of the ring net and cables, they are simulated with parallel bonds following a linear force-displacement relation (Li et al., 2020; Nicot et al., 2007). In comparison, brake elements exhibit
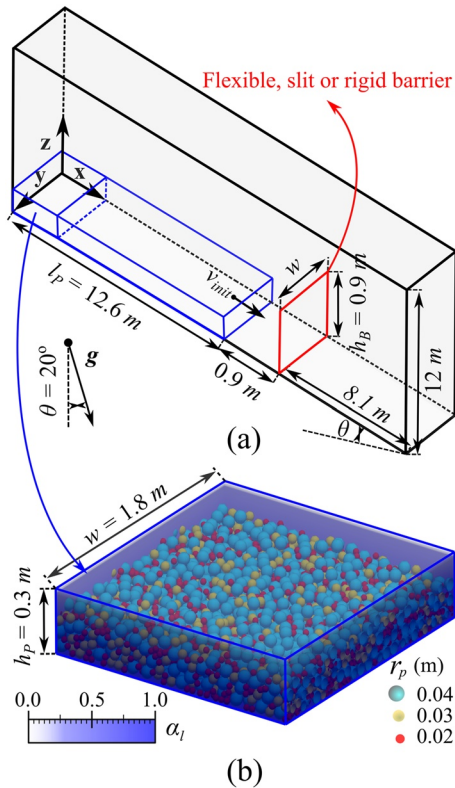
Figure 3. Model setup. (a) Model geometry prior to the release of the solid-liquid mixture; and (b) illustration of a representative part of a mixture sample consisting of tridisperse particles and a viscous liquid. r_p and α_l denote particle radius and liquid volume fraction, respectively.

highly nonlinear behavior and experiences friction and plastic deformation that is modeled by the piecewise linear model (Li et al., 2020; Xu et al., 2018), which captures the changing stiffness of brakes at different load levels. The detailed calibrations with DEM modeling of both quasi-static tensile test on a ring element and dynamic rockfall test on a flexible ring net barrier composed of ring net, cables, and energy dissipators can be found in Li et al. (2020). Moreover, the total physical mass of the ring net and cables is assumed to be lumped over these nodal particles, according to which their density is adjusted. The densities of the nodal particles for the simulated ring element and supporting cables are approximately determined as $\rho_s = 1{,}719$ and 27,320 kg/m^3, respectively. For instance, the density of a nodal particle in a cable is calculated according to the nodal particle radius, the number of nodal particles per meter, and the range of linear mass of supporting cables (0.55–0.98 kg/m) reported by Dugelas et al. (2019). The full model description, calibration, and validation can be found in Li et al. (2020). Key parameters for the modeling of a flexible ring net barrier are summarized in Table 1.

2.3. Model Setup and Simulation Cases

Figure 3a illustrates the model setup for a solid-fluid mixture sample and a resisting barrier constructed on an inclined slope with a slope angle θ. A mixture sample ($h_p = 0.3$ m, $l_p = 12.6$ m, and $w = 1.8$ m) composed of tridisperse particles and viscous liquid (Figure 3b) is initially placed on the top of the flow channel behind a valve wall, which will be uniformly assigned with prescribed initial velocities ($v_{init} = 1$–12 m/s) and released to impact on a flexible, slit or rigid barrier. h_p, l_p, and w are the length, height, and width of the initial sample of impinging flows, respectively. The CFD domain is bounded by an upper atmosphere face, an outlet face at the end of the channel, and 4 no-slip channel walls (Figure 3a). At the initial state, only fluid cells in the mixture sample are filled with liquid, leaving the rest of the CFD domain filled with air. In the DEM simulation, the sides and bottom of the

Table 1
Key Parameters Adopted in the Modeling of Flexible Ring Net Barrier

Items	Properties	Values
Particle in a barrier[a]	Radius (m)	0.003
	Number	14,725
	Density for ring element, cable, and brake (kg/m^3)	7,800, 12,000, and 20,000
	Young's modulus (GPa)	10
	Poisson's ratio	0.3
	Restitution coefficient	0.1
	Friction coefficient	0.1
Bond in a barrier[a]	Normal stiffness of ring element (N/m)	3×10^{11}
	Shear stiffness of ring element (N/m)	9×10^{8}
	Normal stiffness of cable (N/m)	8×10^{11}
	Shear stiffness of cable (N/m)	8×10^{8}
	Stiffnesses of brake at the three stages ($\times 10^{8}$ N/m)	20, 1.3, 3.2
	Force limits of brake at the three stages (kN)	50, 80, 100

[a]Key parameters in the modeling of ring net and cable (Dugelas et al., 2019; Li et al., 2020) as well as brake element (Li et al., 2020; Xu et al., 2018). The bond stiffness here is calculated by multiplying the stiffness per unit area (i.e., $\overline{k}^n$ and $\overline{k}^s$) by the cross-section area of the bond.

Table 2
Key Parameters Adopted in the Modeling of Geophysical Mass Flows

Items	Properties	Values
Particle in a flow	Particle number	28,125
	Density[a] (kg/m^3)	2,650
	Radius (m)	0.02, 0.03, and 0.04
	Young's modulus (particle-particle contact) (GPa)	70
	Young's modulus (particle-wall contact) (GPa)	700
	Poisson's ratio[a]	0.3
	Restitution coefficient[a]	0.4
	Interparticle friction coefficient	0.7
	Particle-wall friction coefficient	0.5
	rolling friction coefficient[a]	0.15
Air[a]	Density (kg/m^3)	1
	Viscosity (Pa•s)	1.48×10^{-5}
Fluid[b]	Density (kg/m^3)	1,350
	Consistency index (Pa•s^n)	21.30
	Flow index	0.24
	Yield stress (Pa)	17.86
Simulation control	Cell size (CFD) (m)	$0.15 \times 0.15 \times 0.15$
	Time step (DEM) (s)	5×10^{-7}
	Time step (CFD) (s)	5×10^{-6}
	Simulated real time (s)	2–12

[a]The typical values of physical properties for geophysical flows (Iverson, 1997). [b]Typical values of the non-Newtonian fluids (Remaître et al., 2005).

flow channel are modeled as fixed, rigid, and frictional walls with Young's modulus 10 times of particles. Note that slit and rigid barriers are modeled as fixed, rigid, and frictional walls in DEM and no-slip boundary walls in CFD. In particular, the slit dam has 4 spacings with spacing length $l_b = 0.15$ m (Figure 4). Its transverse blockage l_b/w and relative post spacing l_b/δ are 33.3% and 1.875, respectively. δ is the maximum diameter of particles.

Different materials in the flow behave differently and govern the flow behavior in a complex way (Heyman et al., 2016; Pudasaini & Mergili, 2019). In this work, a typical two-phase geophysical flow is considered as a mixture of a discrete phase consisting of gap-graded frictional particles and a continuous viscous fluid phase composed of fine-solid and fluid materials. A total of 28,125 particles have been produced for the solid phase of these geophysical flows. The total volume and solid volume concentration ε_s for a geophysical flow are 6.8 m^3 and 0.5, respectively. The mass percentages of the particles with radii r_p equal to 0.04 m, 0.03 and 0.02 m are 70%, 15% and 15%, respectively. The adopted particle sizes of the impacting flows are determined according to the scale of the model setup in Figure 3a. The particle number along the flow width direction needs to be sufficiently large to avoid boundary effect from the lateral walls and meanwhile small enough to save computational cost. The fluid rheological properties of the fluid phase adopt a Herschel-Bulkley fluid (Remaître et al., 2005). Note that the CFD cell size is around two times larger than the maximum particle diameter and several times the average particle diameter, ensuring both the accuracy and stability of the simulations while providing reasonable predictions (Kloss et al., 2012; Shan & Zhao, 2014). Detailed parameters employed in the modeling of geophysical mass flows are summarized in Table 2.

To obtain a comprehensive and systematic analysis of the effects of flow dynamics (*Fr*) on the distinct impact behavior of geophysical flows against flexible, slit, and rigid barriers, the prescribed initial velocities (v_{init}) from 1 to 12 m/s are produced. The obtained range of *Fr* (0.9–7.5) is generally consistent with that of field debris flows, which is from 0.5 to 7.6 (Choi et al., 2015). For convenient discussion, the test IDs are defined according to the group IDs (i.e., barrier types) and v_{init}. FB, SD, and RB denote the test groups with flexible ring net barrier

Table 3
Test Program

Group IDs	FB	SD	RB
v_{init} (m/s)	0.5, 1, 2 , 3, 4, 6, 8, 10, 12, 14	1, 2, 3, 4, 6, 8, 10, 12	1, 2, 3, 4, 6, 8, 10, 12
Fr	0.6~8.7	0.9~7.5	0.9~7.5

system, slit dam, and rigid barrier, respectively. For instance, Case FBV2 denotes the numerical test of geophysical flow with v_{init} = 2 m/s impacting on a flexible ring net barrier. Note that additional FB cases with v_{init} = 0.5 and 14 m/s have been added for the analysis of the *Fr*-dependent load-deflection relations in Section 3.3. The control parameters in the three test groups are summarized in Table 3.

In this study, the large-scale (10^0–10^1 m) simulations, instead of real-scale (10^1–10^2 m) ones, are conducted for computational efficiency, and their dynamic similarity with real-scale geophysical flows is guaranteed by Froude similarity (Li et al., 2021; Wendeler et al., 2019). The DEM time step is determined according to the constraint of Rayleigh time (Smuts et al., 2012), whilst the CFD time step is adopted based on the coupling interval between CFD and DEM. Following Li et al. (2020), we exchange information between CFD and DEM computations every 10 time steps of DEM to ensure balanced accuracy and efficiency. For each simulation case with the flexible barrier, the computation time on an 8-core Intel CPU (3.7 GHz) desktop computer varies from 90 to 390 hr, mainly depending on the simulated real time (2–12 s). The number of elements or particles in a flexible barrier can be reduced by considering structural symmetry (e.g., Albaba et al., 2017; Kong, Li, & Zhao, 2021). However, such simplifications may result in unrealistic force sharings and transitions, and thus barrier deformations, as discussed in Text S4 in Supporting Information S1. The size of the simulated flexible barrier is determined according to the scale of the setup in Figure 3a. The barrier ring net size (i.e., ring diameter d_r = 70 mm) is determined to block large particles in a flow while allowing small particles to pass through, which recovers the major function of a flexible barrier in reality. Nonetheless, this reduced-sized flexible barrier will certainly affect its permeability, deformability, and mechanical characteristics. In this work, we intend to find a balance between computational efficiency, accuracy, and the primary objective, which requires incoming flows with adequate flow volume and varying *Fr* conditions.

3. Results and Discussion

3.1. Impact Dynamics Under Pile-Up and Runup Modes

Figure 4 shows the comparison of key flow-barrier interactions of two-phase geophysical flows against flexible, slit, and rigid barriers via pile-up (v_{init} = 2 m/s) and runup (v_{init} = 4 m/s) impact modes. It is seen that partial materials of the impinging flows can pass through both flexible and slit barriers, compared with the closed-type rigid barrier. Some particles emerge from the fluid surface (α_l = 0.5) for FB cases at impact stages *II* and *III* (Figures 4a and 4d), which is not observed for SD cases (Figures 4b and 4e). This indicates that the barrier permeability of FB cases is higher than SD cases in this work. Moreover, the simulated flexible ring net barrier can significantly deform during the impact process (Figures 4a and 4d). The comparisons of key flow-barrier interactions and barrier deformations between numerical predictions and both experimental and field observations for flexible ring net barriers can be found in Figures S2 and S3 in Supporting Information S1.

For pile-up impact (the middle panel of Figures 4a–4c), the trapezoid-shaped or wedge-like dead zones (Faug et al., 2009; Kong, Zhao, & Li, 2021) are observed after a flow with relatively slow dynamics (v_{init} = 2 m/s) impacts flexible, slit and rigid barriers at stage *II*. The flowing layer may hardly directly impact a barrier before settling down to form a new layer of the dead zone. In contrast, under runup impact (the middle panel of Figures 4d–4f), the flow fronts with relatively fast dynamics (v_{init} = 4 m/s) impact onto the barrier and then shoots up along the barrier at stage *II*, during which the triangle-shaped or ramp-like dead zones are observed. At stage *III* (the lower panel of Figure 4), the dead zone under either pile-up or runup impact mode is enlarged as more overlying debris mass is deposited with a shape (i.e., trapezoid or triangle) largely similar to that in stage *II*. Clear differences between the two impact modes for three types of barriers can be observed in supplementary videos (https://doi.org/10.5281/zenodo.6577214) (Kong et al., 2022). Nonetheless, the recognition between pile-up and runup modes is never as simple as illustrated in Figures 1 and 4, but depends on a wide range of impinging
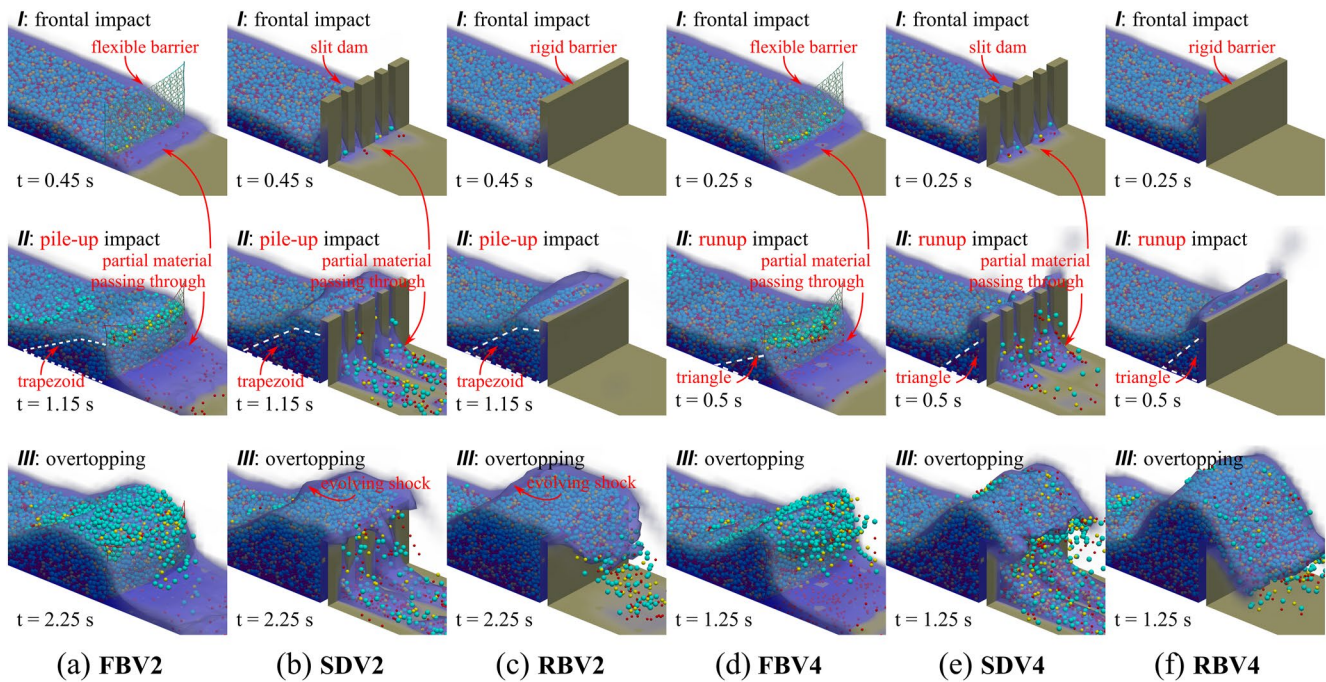
Figure 4. Comparison of the key flow-barrier interactions at three stages (i.e., frontal impact, pile-up or runup impact, and overtopping) via two impact modes: pile-up impact for geophysical flows (v_{init} = 2 m/s) against (a) flexible, (b) slit, and (c) rigid barriers; runup impact for geophysical flows (v_{init} = 4 m/s) against (d) flexible, (e) slit, and (f) rigid barriers. The white dash-dotted lines represent the approximate boundaries of dead zones. The fluid part in geophysical flows is visualized by the contour surface of the liquid phase with α_l = 0.5 and in the background color with transparency equal to 50%.

flow conditions (flow dynamics, height, solid fraction, and rheology), geometries (flow, channel and barrier), barrier permeability and deformability, among others. For instance, Faug (2015) proposed a phase diagram for granular-wall interactions, indicating a typical barrier-flow height ratio h_B/h_0 around 3 used in this study brings in the area where a little variation of Fr or h_B/h_0 can produce changes in the dominant pattern (e.g., dead zone, standing jump, and airborne jet) but fully developed bores that can propagate far upstream are unlikely here.

Based on the above analyses, the impact mode, either pile-up or runup, can be tentatively identified for the overall impact process. Note that the impact behavior of a geophysical flow could start with a runup mode and transform into a pile-up mode (Kong, Li, & Zhao, 2021; Song et al., 2017; Zhou, Du, et al., 2020). In this study, we recognize the primary impact mode according to flow features (e.g., dead zone shape and formation, flowing layer behavior) at stage *II* and the beginning of stage *III* when incoming flows remain adequate. It is anticipated that the impact mode transitions from runup to pile-up eventually occur owing to less kinetic energy carried by subsequent incoming flows and rearrangements in the quasi-static zone formed upstream. Quantifying this transition needs further investigation, which is beyond the scope of this study. Importantly, Figure 4 indicates that impact mode transitions from pile-up to runup occur in the cases with 2 m/s < v_{init} < 4 m/s for flow-resisting flexible, slit and rigid barriers in this study. This serves as a basis in the discriminant of pile-up and runup regimes in Figures 7, 8 and 10. Further identification of the impact modes for Cases FBV3, SDV3, and RBV3 (v_{init} = 3 m/s) may need quantitative examinations of both flow features (dead zone shape and formation, overtopping behavior) and barrier responses, as investigated by Kong, Li, and Zhao (2021).

Moreover, Figures 4b and 4c indicate that the evolving shocks or reflected waves have been well captured in the SD and RB cases under pile-up modes. Indeed, the pre-impact velocity v_0, the barrier-flow height ratio h_B/h_0, barrier types and geometries will affect the formation of reflected waves (Hu et al., 2020; Kong, Li, & Zhao, 2021). No reflected wave has been observed in Case FBV2 mainly due to high barrier permeability and relatively small h_B/h_0. When subjected to the flow impact, a flexible barrier can reduce in height, which in turn influences barrier containment capacity and further affects both the load acting on the barrier and the barrier deformation. For a slit or flexible wall, downstream flow is possible through the spacings or holes (Figure 4),
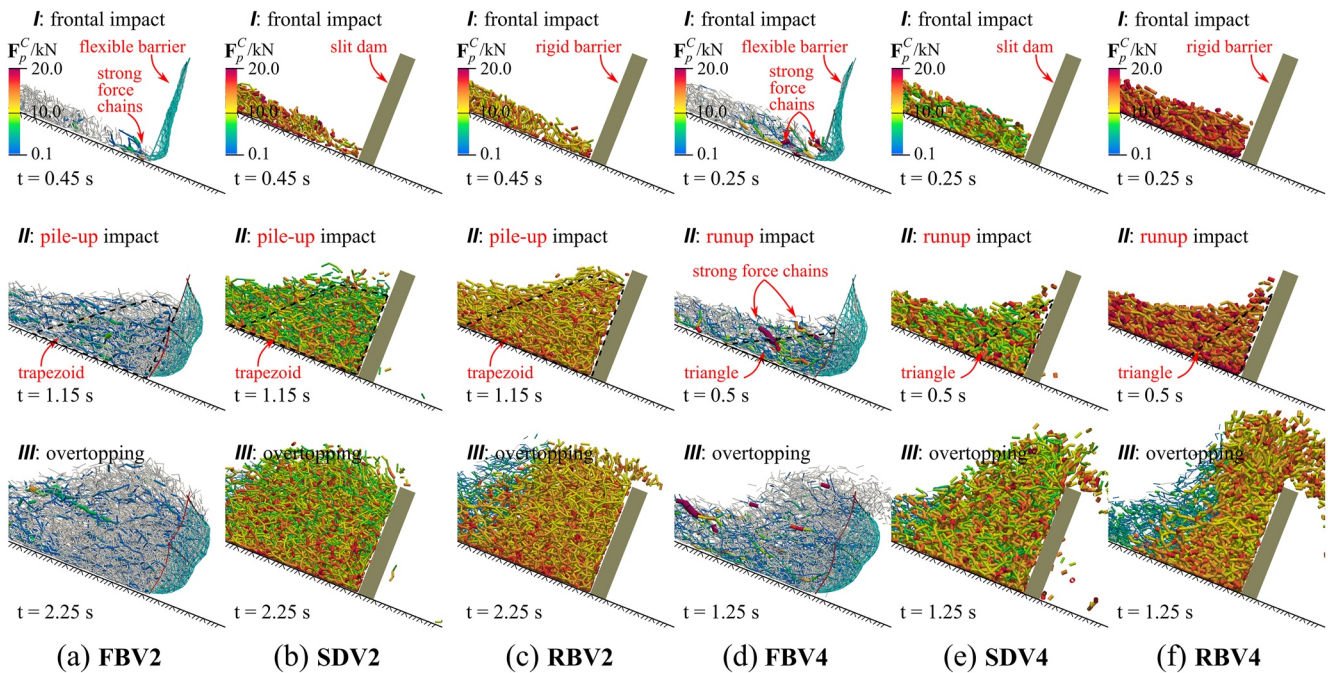
Figure 5. Comparison of the solid-barrier interactions in terms of contact fabric networks at three stages (i.e., frontal impact, pile-up or runup impact, and overtopping) via two impact modes: pile-up impact for geophysical flows ($v_{\text{init}} = 2$ m/s) against (a) flexible, (b) slit, and (c) rigid barriers; runup impact for geophysical flows ($v_{\text{init}} = 4$ m/s) against (d) flexible, (e) slit, and (f) rigid barriers. The black dash-dotted lines represent the approximate boundaries of dead zones. The magnitude of interparticle contact force $\mathbf{F}_p^C$ is denoted by the thickness and color of tubes.

which may attenuate the ability of the bore (Faug, 2015) or dead zone to propagate upstream and then maintain the vertical jet or runup regime over a larger time duration (Figures 4d and 4e).

Corresponding to Figure 4, the comparison of the solid-barrier interactions in terms of contact fabric networks has been further presented in Figure 5. Strong contact forces are denoted in red and are relatively thicker than weak contact forces in blue. The average and maximum contacts upstream of the barrier for RB cases are the largest, while that for FB cases are the smallest (Figure 5). This indicates that flexible barriers can largely reduce the solid-barrier contacts compared with both slit and rigid barriers. At stage *I*, strong force chains (red thicker tubes in Figure 5) are observed at the bottom of barriers. Then, metastable dead zones are formed wherein the interparticle contact forces restrict retained particles from moving, presenting mechanically stable contact networks at stage *II*. At stage *III*, strong contact chains mainly occur at both the lower and higher parts of dead zones and the top of the three barriers. Notably, both the static load induced by the dead zone (dominated at stage *III*) and the dynamic load (dominated at stages *I* and *II*) resulting from the flowing debris can be transferred through the contact networks to barriers. The relative dominance played by the static or dynamic load via pile-up and runup modes at different stages will be discussed in the following Section.

3.2. Solid-Liquid Impact Loads and Peak Load Reductions

Key flow-barrier interaction forces along x-direction are extracted from our numerical results, including the solid-barrier contact force F_{s-b}, the fluid-barrier interaction force F_{f-b}, and their summation F_b, that is, total normal impact load acting on a barrier. In particular, for FB cases, $Fb = \sum_{j \in N_b} F_{s-b}^j + \sum_{j \in N_b} F_{f-b}^j$, where F_{s-b}^j and F_{f-b}^j denote F_{s-b} and F_{f-b} acting on a barrier nodal particle j, respectively. N_b is the total number of nodal particles in the barrier. For both slit and rigid barriers, F_{f-b} and F_{s-b} are extracted from the pressures of boundary cells in CFD module and particle-wall interaction forces in DEM module, respectively. Figure 6 compares the temporal evolutions of F_{s-b}, F_{f-b}, and F_b acting on flexible, slit, and rigid barriers via pile-up and runup modes. Large oscillations of F_b are observed in both SD and RB cases, whilst the trends of F_b for FB cases are relatively smooth (Figure 6). This is mainly caused by the load-attenuation mechanism of flexible barriers originating from
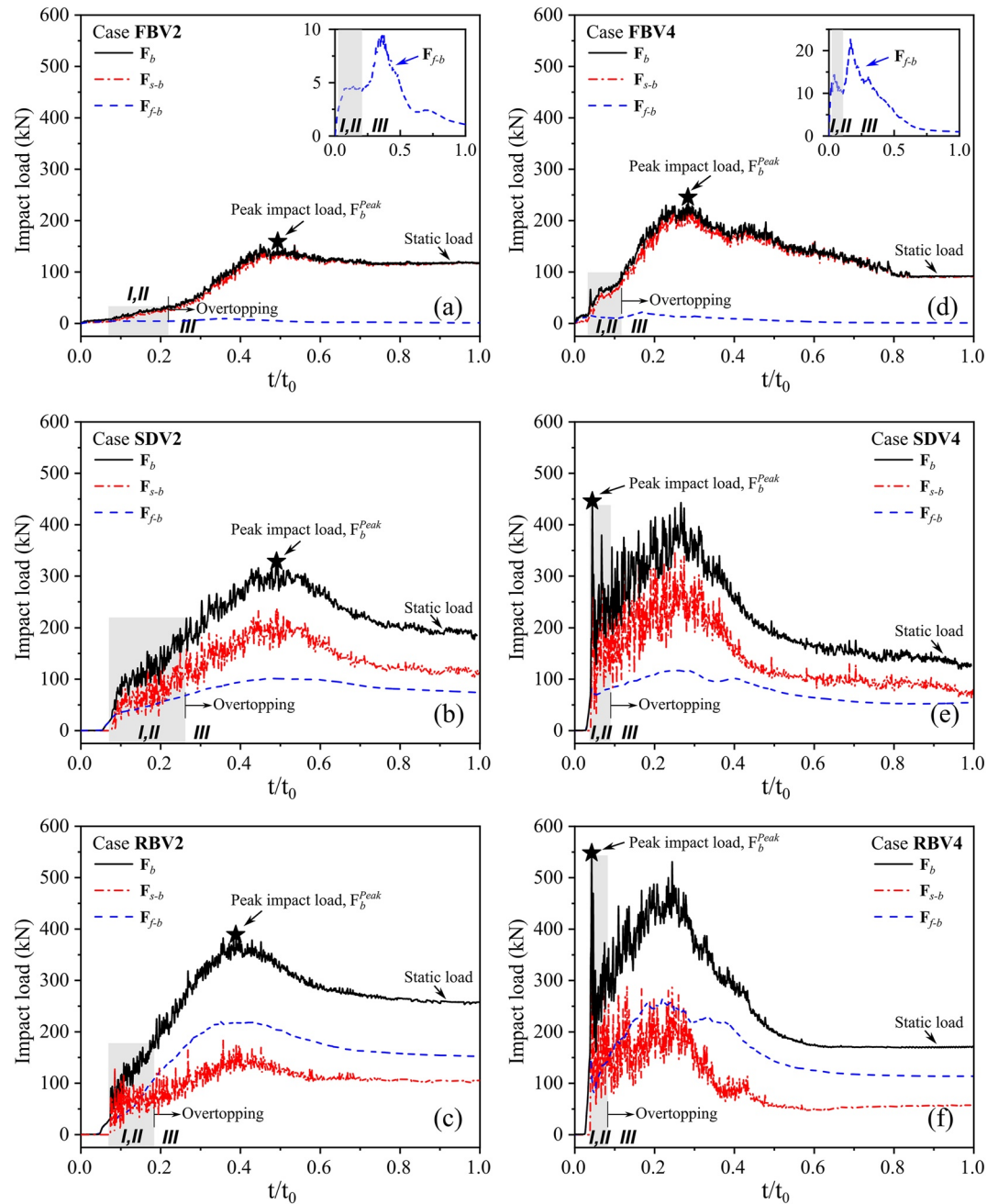
Figure 6. Evolutions of the solid-barrier contact force F_{s-b}, the fluid-barrier interaction force F_{f-b}, and total impact load F_b under pile-up (a, b, and c; $v_{init} = 2$ m/s) and runup (d, e, and f; $v_{init} = 4$ m/s) modes for flexible, slit, and rigid barriers in intercepting two-phase geophysical flows. The gray regions represent the impact durations for stages *I* and *II*.

barrier deflection and extended interaction duration. The force fluctuations of F_b are induced by F_{s-b} since F_{f-b} is very smooth. Similar phenomena have been recorded in centrifuge tests with both rigid and flexible barriers (Song, Choi, Zhou, et al., 2018; Song et al., 2019).

It is seen that the peak impact loads $F_b^{Peak} = \text{Max}(F_b)$ for FB cases under both pile-up and runup modes occur at stage *III* (Figures 6a and 6d). In contrast, F_b^{Peak} for both SD and RB cases takes place at stage *III* under pile-up mode (Figures 6b and 6c) and at stages *I* and *II* under runup mode (Figures 6e and 6f). This implies that stage *III* can be critical for the estimation of F_b^{Peak} for FB cases via two impact modes. For SD and RB cases, stage *III* is important under pile-up mode, whilst stages *I* and *II* are critical under runup mode for predicting F_b^{Peak}. In

addition, two pieces of bulge trend are observed for SD and RB cases under runup mode (Figures 6e and 6f). The first peak bulge is primarily due to the direct impact load acting on barriers at stage *I*, whilst the second bulge is possibly caused by the increasing static load induced by dead zone and shear stress resulting from the flowing layer at stage *III*. Moreover, at the beginning of stage *III*, F_{s-b}, F_{f-b}, and F_b in all cases indicate a striking increase until F_b reaching the peaks. It is due to the increase of static load induced by the dead zone as well as more shear stress and earth pressure induced by the flowing layer transferred through dead zone to barriers. After the peak F_b at stage *III*, F_{s-b}, F_{f-b}, and F_b experience a continuous decrease owing to less kinetic energy carried by subsequent tail flows and a reduction of static load resulting from drained debris cone upstream of flexible and slit barriers. All flow-barrier interaction forces tend to be stable (the so-called static load) as the debris mass becomes stationary in the subsequent filling process.

Quantifying the individual contribution of the solid and the fluid in impinging flows on the total impact load may provide insights into F_b^{Peak}. For FB cases (Figures 6a and 6d), the solid-barrier contact force F_{s-b} is around 10 times larger than the fluid-barrier interaction force F_{f-b} at F_b^{Peak} via two impact modes. For SD (Figures 6b and 6e), F_{s-b} is more than twice under pile-up mode and more than quadruple under runup mode of F_{f-b} at F_b^{Peak}. This indicates that F_{s-b} is the dominated impact load at F_b^{Peak} in both FB and SD cases resulting from the permeability of barriers. By contrast, for RB cases (Figures 6c and 6f), F_{f-b} is around 1.5 times larger than F_{s-b} at F_b^{Peak} under pile-up mode, whilst F_{s-b} is around 3 times larger than F_{f-b} at F_b^{Peak} under runup mode. Figure 6c depicts the dominated load acting on a rigid barrier under pile-up mode changes from F_{s-b} to F_{f-b} after the flow-barrier interactions come into the overtopping process.

Moreover, $T^{I,II}$ represents the impact duration for stages *I* and *II* before overtopping (gray regions in Figure 6). The RB cases experience the shortest $T^{I,II}$ via two impact modes. SD case experiences the longest $T^{I,II}$ under the pile-up mode, whilst FB case presents the longest $T^{I,II}$ under runup mode. Further quantifications of $T^{I,II}$ for all cases will be presented and discussed in the following Section. Figure 6 partly reveals the different intercepting mechanisms of three barriers by numerical quantifications on the individual contribution of the fluid and the solid on the total impact. Therefore, this physically based method helps to connect the microscale flow-barrier interactions with the macroscopic impact behavior for flexible, slit and rigid barriers.

Figure 7 further compares the peak impact loads F_b^{Peak} (left-hand *y* axis) for geophysical flows against flexible, slit and rigid barriers, which allows clarifying the inter-twined relationships among the flow dynamics, barrier types, and peak impact loads for the first time. Note that the impact mode transitions occur at Cases FBV3, SDV3, and RBV3 in this study (indicated by Figure 4). It indicates that F_b^{Peak} is positively correlated with the *Fr* of impinging flows. With the rise of *Fr*, F_b^{Peak} rapidly grows for RB cases, while F_b^{Peak} only experiences a slight increase for FB cases. Figure 7 indicates that F_b^{Peak} for RB cases are always larger than that for both FB and SD cases under the same *Fr* conditions. The F_b^{Peak} reductions for both FB and SD cases are therefore further normalized by the F_b^{Peak} for RB cases. The peak load reduction ratios for both flexible and slit barriers are calculated by $\xi_{\text{FB}} = \left(F_{b,\text{RB}}^{\text{Peak}} - F_{b,\text{FB}}^{\text{Peak}} \right) / F_{b,\text{RB}}^{\text{Peak}}$ and $\xi_{\text{SD}} = \left(F_{b,\text{RB}}^{\text{Peak}} - F_{b,\text{SD}}^{\text{Peak}} \right) / F_{b,\text{RB}}^{\text{Peak}}$, respectively. In addition, ξ_{FB} obtained from 14 centrifuge tests with bouldery and the boulder-debris mixture flows (Song, Choi, Zhou, et al., 2018; Song et al., 2019) and ξ_{SD} measured from dry granular flow against open-type dams (Choi et al., 2020) have been plotted for comparison in Figure 7. We can see that ξ_{FB} extracted from the numerical results in this study ranges from 0.63 to 0.89, which is overall consistent with the estimation of ξ_{FB} ranging from 0.54 to 0.96 obtained from centrifuge tests by Song et al. (2019). Note that dry boulder-debris mixture flows with varying δ/h_0 (0.07~1) against an impermeable flexible barrier made by membrane are performed by Song et al. (2019). δ is the maximum diameter of particles. Consequently, the differences in both impinging flows and resisting flexible barriers cause discrepancies of ξ_{FB} under similar *Fr* conditions.

Moreover, as the *Fr* increases, ξ_{FB} slightly grows from 65% to 70% under pile-up mode, and significantly increases from 70% to 92% under runup mode
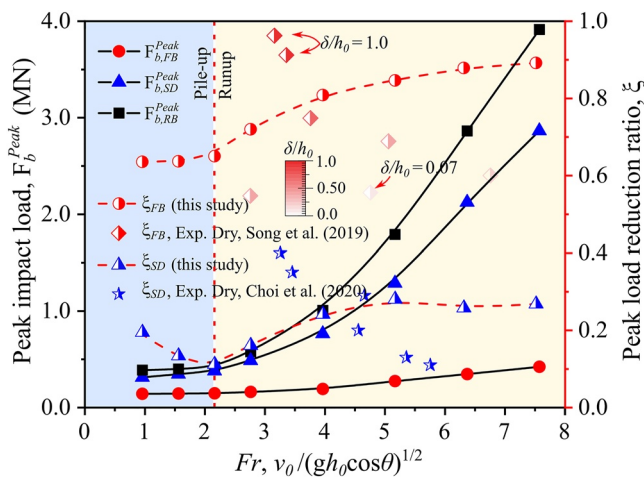
Figure 7. Measured relationships between *Fr*, F_b^{Peak}, and ξ for geophysical flows against flexible, slit, and rigid barriers. The blue and yellow regions denote the pile-up and runup impact modes, respectively. The color of half-solid diamonds represent the normalized boulder diameter δ/h_0 of impinging flows performed by Song et al. (2019).
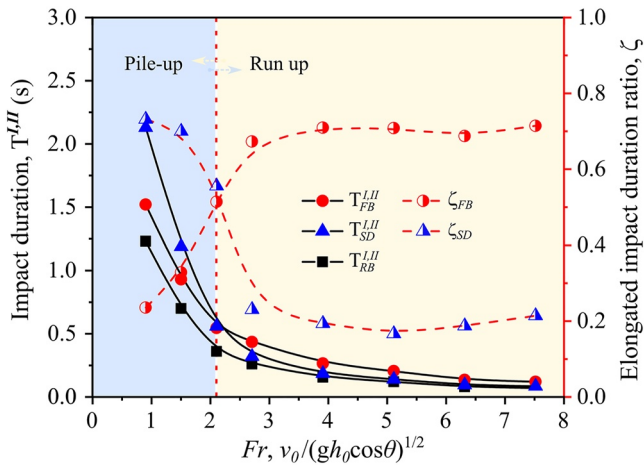
Figure 8. Measured relationships of Fr, $T^{I,II}$, and ζ for geophysical flows against flexible, slit, and rigid barriers. The blue and yellow regions represent the pile-up and runup impact modes, respectively.

(right-hand y axis in Figure 7). It implies that a flexible barrier becomes more effective in the reduction of F_b^{Peak} after the dominated impact mode transitions from pile-up into runup. By contrast, ξ_{SD} slightly decrease from 22% to 18% under pile-up mode and increase from 18% to 38% under runup mode with increasing the Fr. After the transition of impact modes from pile-up to runup, a flexible barrier can significantly reduce F_b^{Peak} relative to a rigid barrier by its high permeability and large structural deformations. In addition to barrier permeability, ξ_{FB} are around 2–3.5 times larger than ξ_{SD}, owing to the structure deformability. This unique load-deflection behavior will be quantitatively examined below (Figure 9). As a result, flexible barriers perform the best in terms of ξ_{FB} (up to 92%), especially under runup mode.

3.3. Elongated Impact Durations and *Fr*-Dependent Load-Deflection Patterns

Figure 8 shows the measured relationships between Fr and $T^{I,II}$ (left-hand y axis). $T^{I,II}$ is defined as the summation of impact durations at stages I and II, before reaching the overtopping process. It is crucial for the compression rate of impinging debris upstream of the barrier and thus F_b^{Peak}. Note that the initial impact with no obvious dead zone forming upstream of the barrier is called the frontal impact (stage I), which can hardly be differentiated accurately from the subsequent pile-up or runup process (stage II). It is found that the $T^{I,II}$ for flexible barrier ($T_{FB}^{I,II}$), slit dam ($T_{SD}^{I,II}$) and rigid barrier ($T_{RB}^{I,II}$) sharply decrease with increasing Fr. As expected, $T_{RB}^{I,II}$ is always shorter than that for both FB and SD cases. Interestingly, $T_{SD}^{I,II}$ is much longer than $T_{FB}^{I,II}$ under pile-up mode, whilst $T_{SD}^{I,II}$ becomes slightly shorter than $T_{FB}^{I,II}$ under runup mode. It is mainly due to that barrier permeability is reduced by high impinging flow discharges and the structure deformability of the FB case is more effective with fast impact dynamics. Moreover, relative to RB cases, the elongated impact duration ratios ζ for FB cases $\zeta_{FB} = \left(T_{FB}^{I,II} - T_{RB}^{I,II}\right)/T_{RB}^{I,II}$ are smaller than that for SD cases $\zeta_{SD} = \left(T_{SD}^{I,II} - T_{RB}^{I,II}\right)/T_{RB}^{I,II}$ under pile-up mode, whilst ζ_{FB} becomes larger than ζ_{SD} under runup mode. As the Fr increases, ζ_{FB} increases tremendously from 22% to 70% until Fr reaches 2.7, and keeps relatively constant at a high level (~70%) within $2.7 < Fr \leq 7.5$, in contrast to the trend of ζ_{SD}. A larger Fr seems to weaken the permeability of a slit dam due to a larger flow discharge resulting in a faster formation of a dead zone, while it can strongly strengthen the maximum deformation of a flexible barrier (see Figure 9). Compared with a slit dam, a flexible barrier presents a much larger ζ ($\zeta_{FB} \cong 3\zeta_{SD}$) under the runup mode, owing to its effective load-deflection behavior can prolong impact duration and reduce compression of the debris assembly upstream of the barrier, thereby performing the largest ξ (Figure 7).

Figure 9 presents the Fr-dependent $F_b–D_h$ relations of a flexible ring net barrier against geophysical flows to explore the load-attenuation mechanism of a flexible barrier. Three load-deflection patterns can be concluded as follows. In pattern I (Figure 9a), the two-stage development trend of the $F_b–D_h$ relations with $Fr \leq 1.5$ for three pile-up cases are generally consistent with each other. The equivalent barrier stiffness k_B^n denotes the assumed linear increasing rate of the $F_b–D_h$ relations, which experiences two major stages before F_b^{Peak}: $k_{B,I}^n$ at the initial deformation stage and $k_{B,II}^n$ at the subsequent deformation stage. Initially, $k_{B,I}^n$ does not play a significant role until D_h reaches the inflection point since the entire structure behaves flexibly. After the inflection point, the stiffness increases sharply to $k_{B,II}^n$, owing to the majority of the flexible features have subsequently been exhausted. Specifically, when the rings have plastically deformed and most brake elements have been applied, the entire structure gets progressively stiffer until $k_{B,II}^n$ reaches a specific value and begins to approach a smaller stiffness.

In pattern II (Figure 9b), the initial development of $F_b–D_h$ with relatively small barrier deflection becomes much more complicated with $Fr \geq 2.1$. As expected, the barrier deflections present a distinct behavior when impact modes transition from pile-up to runup. Because the solid-liquid flow evolutions and structure deformations are tightly coupled during a debris flow against a flexible barrier. Both k_B^n and F_b in Case FBV3 presents an increasing-decreasing trend before the inflection point at $D_h = 0.3$. Then, F_b rapidly increases to the peak with a relatively large $k_{B,II}^n$. Moreover, the timing and magnitude of the first peak of F_b are respectively negatively
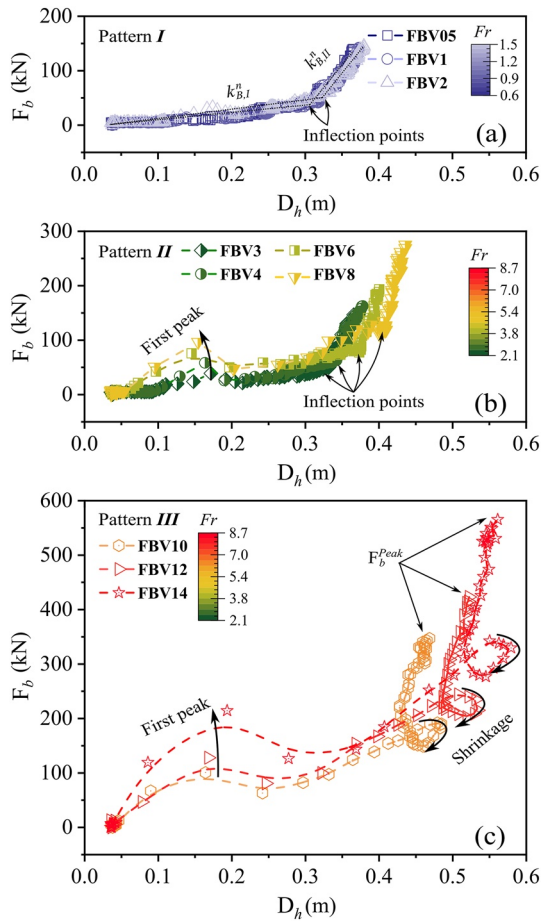
Figure 9. The Fr-dependent load-deformation ($F_b - D_h$) relations of a flexible ring net barrier in arresting geophysical flows for (a) pattern I, (b) pattern II, and (c) pattern III. F_b and D_h denote the flow-direction impact load sustained by the barrier and the maximum flow-direction barrier deflection, respectively.

and positively correlated with Fr. Interestingly, in pattern III (Figure 9c), when the impacting flow dynamics is extraordinarily high ($Fr \geq 6.3$ and $v_{init} \geq 10$ m/s), the backward development trend of D_h near the inflection point can be observed within a certain duration. This implies that the barrier will begin to shrink after reaching the maximum barrier deflection along with a slight decrease of barrier load within a certain duration. It is mainly due to the excessive deformation of the barrier in the direction of the flow, which has been also observed by the large-scale flume tests conducted by DeNatale et al. (1999). Details of the measured barrier deflections from the USGS flume tests can be found in Figure S4 in Supporting Information S1. To the best of the authors' knowledge, there remains no detailed observation on this interesting phenomenon.

Moreover, Figure 9 indicates that the Fr has a strong and positive correlation with the maximum values of F_b and D_h, which are the key considerations for designing flexible barriers. In addition, the energy dissipation during a flexible barrier arresting a geophysical flow includes the energy dissipated in impinging flow (e.g., frictional slidings, collisions, and viscous shearing in both flowing layer and dead zone) and the energy absorbed or dissipated by the barrier (e.g., barrier strain energy and frictional slidings within the barrier). The areas below the $F_b - D_h$ lines could be calculated to estimate the barrier strain energy. Specifically, assuming a linear increase of the barrier load F_b, plotted over the deformation D_h, produces the barrier strain energy with F_b^{Peak}. Therefore, quantitative examinations of the $F_b - D_h$ relations may provide a new way to quantify the barrier strain energy and thus enhance our understanding of this complex energy dissipation process. In reality, barrier deflection is a 3D phenomenon varying across the width and height of the barrier (see Figure S4 in Supporting Information S1). The definition of D_h is idealized. The complicated evolution of barrier deformations strongly depends on the competitive roles of the three major load components during three stages, including the static load induced by the trapped debris (dead zone), the dynamic load from the impinging flow, and the drag or shear load from the flowing layer above dead zone. In addition to the flow dynamics, the $F_b - D_h$ relations could differ with varying barrier deformability and configurations (e.g., number of supporting cables, mesh type, activation force of brakes), which need to be further explored in the future.

3.4. A Unified Barrier-Specific Design Diagram

Figure 10 presents a unified design diagram to quantify the influences of Fr, barrier permeability and barrier deformability on hydrostatic coefficient κ, hydrodynamic coefficient α and the normalized maximum runup height h_{max}/h_0 for flexible, slit and rigid barriers in arresting geophysical flows. κ and α are critical coefficients in popular analytical models for predicting peak impact pressures. These analytical models, empirical coefficients (κ and α), and the Fr-related models established for rigid and flexible barriers are briefly introduced in Text S6 in Supporting Information S1. To facilitate a comprehensive analysis, a unique data set, comprising normalized data obtained from analytical models (Li et al., 2021; Song, Zhou, et al., 2021), empirical relations (P. Cui et al., 2015), experiments (Armanini et al., 2020; Choi et al., 2020; Hu et al., 2020; P. Cui et al., 2015; Song, Chen, et al., 2021; Song, Zhou, et al., 2021; Vicari et al., 2021), field events (Hübl et al., 2009), practical design values (Armanini, 1997; Hungr et al., 1984; Kwan & Cheung, 2012; Wendeler, 2016) and numerical results, is plotted in Figure 10 for comparison and also summarized in Table S1 in Supporting Information S1.

Figures 10a and 10b indicate that κ and α are found positively and negatively correlated to the Fr, respectively. As the increasing of Fr, the flow inertia dominates over the gravitational force, κ increases rapidly due to the decreasing weight of the static component, while α decreases due to more weight of the dynamic component.
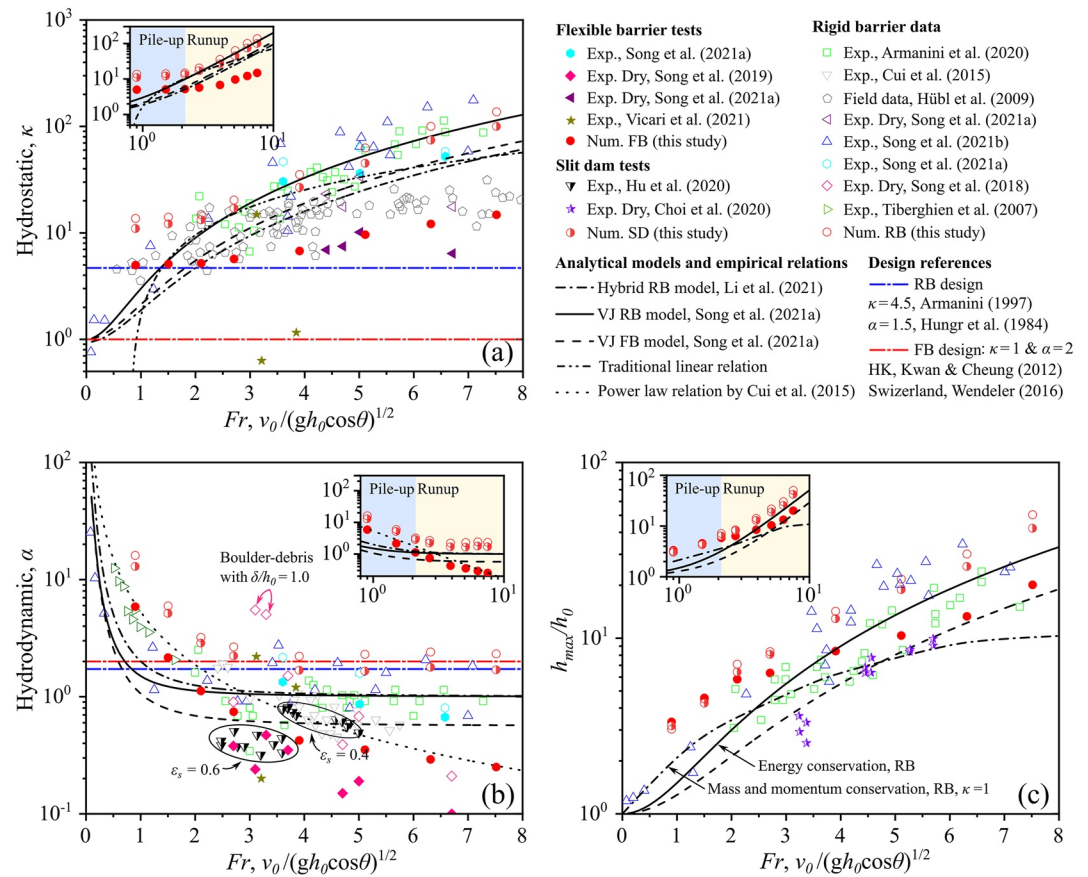
Figure 10. A unified barrier-specific design diagram quantifying the influences of Fr, barrier permeability and structure deformability on the predictions of (a) hydrostatic coefficient κ, (b) hydrodynamic coefficient α, and (c) the normalized maximum runup height h_{max}/h_0, based on the comparison of analytical models, empirical relations, experiments, field events, design values, and numerical results for flexible, slit and rigid barriers in mitigating geophysical flows. Insets use the double-log plots. The blue and yellow regions in insets represent the pile-up and runup modes, respectively.

This reveals an interesting competing mechanism of the hydrodynamic and hydrostatic components for the flow impacts. Moreover, numerical predictions of Fr-κ and Fr-α for FB cases differ significantly from both SD and RB cases (Figure 10), especially under runup mode ($Fr > 2.1$). It is interesting to observe a continuously decreasing trend of α for FB cases when $Fr > 3.9$, which corresponds well to a more effective load-deflection behavior of a flexible barrier (Figure 9). The discrepancy between analytical models and our FB cases is mainly due to their idealized assumptions, such as the ignorance of outlet materials and no energy dissipations. Notably, the Fr-α relation predicted by an empirical power law (P. Cui et al., 2015) agrees well with our FB cases (Figure 10b), while its trend differs essentially from current analytical models and our SD and RB cases, especially when Fr is larger than 3.9.

The insets in Figures 10a and 10b show that the Fr-κ relation predicted by the hybrid RB model (Li et al., 2021) agrees well with both SD and RB cases under runup mode ($Fr \geq 2.1$), while the Fr-α relations predicted by analytical models differ significantly with our SD and RB cases. Under the pile-up mode ($Fr < 2.1$), κ and α extracted from SD and RB cases are much higher than analytical model predictions and experimental estimations (Figures 10a and 10b). This is likely caused by that the F_b^{Peak} with $Fr < 2.1$ strongly depends on the progressive accumulation of trapped debris and the flowing layer upon the dead zone at the overtopping process (see the lower panel in Figure 4), whilst experimental tests with slow impact dynamics (i.e., pile-up mode) commonly perform impinging flows regardless of overflow (e.g., Armanini et al., 2020; Hu et al., 2020; Song, Chen, et al., 2021; Song, Zhou, et al., 2021; Tiberghien et al., 2007) and in the absence of large particles (Armanini et al., 2020; Hu et al., 2020; Song, Chen, et al., 2021; Song, Zhou, et al., 2021; listed in Table S1 in Supporting Information S1).

In addition, analytical models mainly focus on the dynamics caused by fast geophysical flows that encounter obstacles broad enough and high enough (Iverson et al., 2016). Moreover, the inset in Figure 10a shows that the conventional linear fitting curve ($\kappa = 7.8 \times Fr - 6.3$) deviates apparently from the non-linear dependence of κ on Fr (especially under pile-up mode), while κ begins to increase significantly after impact modes transition from pile-up to runup ($Fr \geq 2.1$).

Moreover, the Fr-α relations extracted from SD and RB cases are much larger than those obtained from experiments, empirical relations and analytical models (Figure 10b), especially under runup mode. It is possibly due to that the maximum particle diameter $\delta = 80$ mm adopted in this study is much larger than δ used by experiments (0.6–20 mm; listed in Table S1 in Supporting Information S1; Armanini et al., 2020; Hu et al., 2020; P. Cui et al., 2015; Song, Chen, et al., 2021; Song, Zhou, et al., 2021). Meanwhile, both empirical relations and analytical models are obtained or calibrated based on these experiments. Notably, two data points obtained from centrifuge tests with bouldery and the boulder-debris mixture flows (Song, Choi, Zhou, et al., 2018) are higher than our SD and RB cases. In their centrifuge tests, a glass sphere with $\delta = 0.039$ m is equivalent to a prototype boulder with $\delta = 0.87$ m under an elevated gravitational acceleration condition (22.4 g). Song, Choi, Zhou, et al. (2018) suggested that for those $\delta/h_0 > 0.6$, single boulder impact should be considered separately using Hertz equation (Hungr et al., 1984) rather than hydraulic models with κ or α. Note that this work takes no account of huge boulders, which are frequently observed in natural debris flows (Iverson et al., 2011; Ng et al., 2021; Zhang et al., 2021). These boulders could greatly gain high destructive power and significantly differ the impact behavior.

Despite the nonlinear relationships for both Fr-κ and Fr-α, constant hydrostatic and hydrodynamic coefficients are widely used for the practical design of various flow-resisting barriers. For rigid barrier designs, $\kappa = 4.5$ recommended by Armanini (1997) and $\alpha = 1.5$ suggested by Hungr et al. (1984), are widely adopted. However, adopting $\kappa = 4.5$ and $\alpha = 1.5$ might result in unsafe rigid barrier designs since our numerical results and some of the experiments and analytical model predictions are above the line $\kappa = 4.5$ with $Fr \geq 2.1$ (Figure 10a) and the line $\alpha = 1.5$ with $Fr < 2.1$ (Figure 10b). For the design of flexible barriers, $\kappa = 1$ and $\alpha = 2$ are suggested in Switzerland (Wendeler, 2016) and Hong Kong (Kwan & Cheung, 2012). Figures 10a and 10b indicate that using $\kappa = 1$ might result in unsafe designs while using adopting $\alpha = 2$ shall be sufficient to cover most of the scenarios with $Fr > 1.5$. Therefore, constant values for κ and α are certainly strong approximations that may lead to over-design or under-design. Figures 10a and 10b indicate that both κ and α are not constant numbers. Models with analytic expressions involving both κ and α are needed. For instance, there are well-established analytical models (Albaba et al., 2018; Faug et al., 2012), calculating the impact pressure as the sum of a hydrostatic contribution and an inertial contribution for granular-wall interactions.

Furthermore, κ extracted from rigid barrier tests by Song, Chen, et al. (2021) with dry sand flows is much smaller than that for sand-water flows (Figure 10a), while α obtained from slit dam tests by Hu et al. (2020) using cobblestone-glass-water flows with $\varepsilon_s = 0.4$ is higher than those with $\varepsilon_s = 0.6$ (Figure 10b). This implies that the ε_s of an impinging flow presents a negative correlation with its F_b^{Peak} under certain circumstances. Therefore, the particle size distribution (especially large particles) and solid concentration ε_s (from dry sand to pure water flows) also have substantial effects on both κ and α. However, current analytical models commonly regard typical two-phase geophysical flows as single-phase flows (Iverson et al., 2016; Li et al., 2021). The findings highlight that proper determinations of anticipated flow properties (solid concentration, particle size distribution, and boulder size) may weigh over the selection of appropriate analytical models. In addition, the discrepancy among analytical model predictions, experiments, and our numerical results motivates us to further consider and examine the effects of anticipated flow properties, barrier permeability, and structure deformability on the impact responses.

Figure 10c shows that the discrepancy of $h_{\max}/h_0$ between analytical model predictions and our numerical results is obvious when $Fr < 2.1$, while they tend to converge with each other with $Fr \geq 2.1$ (Figure 10c). When $Fr < 2.1$ (pile-up mode in this study), the numerical predictions of $h_{\max}/h_0$ are much larger than that obtained from experiments and analytical models. In this work, the $h_{\max}/h_0$ under pile-up mode mainly depends on the progressive accumulation of debris upstream of barriers, and the minimum $h_{\max}/h_0$ should be larger than three as the subsequent impinging flows will eventually overtop these barriers. Nonetheless, no overtopping processes are performed by the experiments (Armanini et al., 2020; Choi et al., 2020; Song, Chen, et al., 2021; listed in Table S1 in Supporting Information S1), while analytical models focus on the dynamics of supercritical flows that encounter obstacles broad enough and high enough to stop the downstream flow and cause a lateral redirection

of momentum (Iverson et al., 2016). When $Fr \geq 2.1$ (runup mode in this study), the predictability of analytical models on h_{max}/h_0 is much better than that on peak impact load.

4. Conclusions

In this paper, we provide a systematic analysis of the different intercepting mechanisms of flexible, slit and rigid barriers in arresting two-phase geophysical flows with varying flow dynamics. This has never been achieved in previous studies. The findings in this paper support the following conclusions:

1. A unified modeling framework based on the coupled CFD-DEM method is applied to probe the dynamics of flexible, slit, and rigid barriers in arresting two-phase geophysical flows with varying Fr conditions. In particular, a permeable and deformable flexible barrier consisting of a ring net, cables, and brake elements is modeled, accounting for the ring-ring-cable frictional slidings. The numerical results reasonably capture both experimental and field observations on key flow-barrier interactions and barrier deformations.
2. The differing mechanisms of flexible, slit and rigid barriers via pile-up and runup modes are revealed by quantitative and qualitative characterizations. The individual role of the fluid and solid in flows, the deformability and permeability of different barriers under the two impact modes have been captured. Our findings highlight that flexible barriers perform the best regarding the largest peak load reduction ratios under runup mode, owing to their high permeability and effective load-deflection behavior. Three Fr-dependent load-deflection patterns have been concluded for a flexible barrier for the first time.
3. The study presents a unique data set comprising analytical models, experiments, field events, practical design values, and our numerical results for geophysical flows against flexible, slit, and rigid barriers, quantifying the influences of Fr, barrier permeability, and structure deformability on hydrostatic κ, hydrodynamic α, and the normalized maximum runup height. We find that current analytical models calibrated by idealized experiments may underestimate the peak impact for both slit and rigid barriers owing to the neglect of large particles in impinging flows, and meanwhile overestimate it for flexible barriers due to the poor representations of barrier permeability and deformability. The presented design diagram may offer a possible improvement in analytical model developments and the practical design of flow-resisting countermeasures.

There are future explorative areas on the study of dynamic flow-barrier interactions. In addition to flow dynamics, the flow-barrier interactions can be affected by the barrier-flow height ratio (Faug, 2015), the scale and geometry, barrier permeability, configuration and mesh size of the flexible barrier (Wendeler, 2016; Wendeler & Volkwein, 2015), as well as barrier failures. These crucial aspects will be further explored in the future.

Data Availability Statement

The supplementary videos (Figures 4 and 5) and data set (Figures 6–10) underlying this article are permanently archived at https://doi.org/10.5281/zenodo.6577214 (Kong et al., 2022). The code used to produce the computational fluid dynamics and discrete element method coupling is licensed under GNU and published on GitHub https://github.com/CFDEMproject/CFDEMcoupling-PUBLIC/ (CFDEMproject, 2017).

References

Albaba, A., Lambert, S., & Faug, T. (2018). Dry granular avalanche impact force on a rigid wall: Analytic shock solution versus discrete element simulations. *Physical Review E*, *97*(5), 052903. https://doi.org/10.1103/PhysRevE.97.052903

Albaba, A., Lambert, S., Kneib, F., Chareyre, B., & Nicot, F. (2017). DEM modeling of a flexible barrier impacted by a dry granular flow. *Rock Mechanics and Rock Engineering*, *50*(11), 3029–3048. https://doi.org/10.1007/s00603-017-1286-z

Amini, A., Bollaert, E., Boillat, J. L., & Schleiss, A. J. (2008). Dynamics of low-viscosity oils retained by rigid and flexible barriers. *Ocean Engineering*, *35*(14–15), 1479–1491. https://doi.org/10.1016/j.oceaneng.2008.06.010

Arattano, M., & Franzi, L. J. N. H. (2003). On the evaluation of debris flows dynamics by means of mathematical models. *Natural Hazards and Earth System Sciences*, *3*(6), 539–544. https://doi.org/10.5194/nhess-3-539-2003

Armanini, A. (1997). On the dynamic impact of debris flows. In A. Armanini & M. Michiue (Eds.), *Recent developments on debris flows* (pp. 208–226). Springer.

Armanini, A., Rossi, G., & Larcher, M. (2020). Dynamic impact of a water and sediments surge against a rigid wall. *Journal of Hydraulic Research*, *58*(2), 314–325. https://doi.org/10.1080/00221686.2019.1579113

Ashwood, W., & Hungr, O. (2016). Estimating total resisting force in flexible barrier impacted by a granular avalanche using physical and numerical modeling. *Canadian Geotechnical Journal*, *53*(10), 1700–1717. https://doi.org/10.1139/cgj-2015-0481

Breard, E. C., Dufek, J., Fullard, L., & Carrara, A. (2020). The basal friction coefficient of granular flows with and without excess pore pressure: Implications for pyroclastic density currents, water-rich debris flows, and rock and submarine avalanches. *Journal of Geophysical Research: Solid Earth*, *125*(12), e2020JB020203. https://doi.org/10.1029/2020JB020203

Brighenti, R., Segalini, A., & Ferrero, A. M. (2013). Debris flow hazard mitigation: A simplified analytical model for the design of flexible barriers. *Computers and Geotechnics*, *54*, 1–15. https://doi.org/10.1016/j.compgeo.2013.05.010

Bugnion, L., McArdell, B. W., Bartelt, P., & Wendeler, C. (2012). Measurements of hillslope debris flow impact pressure on obstacles. *Landslides*, *9*(2), 179–187. https://doi.org/10.1007/s10346-011-0294-4

CFDEMproject. (2017). CFDEMcoupling-PUBLIC [Software]. GitHub. Retrieved from https://github.com/CFDEMproject/CFDEMcoupling-PUBLIC.git

Choi, C. E., Ng, C. W. W., Au-Yeung, S. C. H., & Goodwin, G. R. (2015). Froude characteristics of both dense granular and water flows in flume modelling. *Landslides*, *12*(6), 1197–1206. https://doi.org/10.1007/s10346-015-0628-8

Choi, C. E., Ng, C. W. W., Liu, H., & Wang, Y. (2020). Interaction between dry granular flow and rigid barrier with basal clearance: Analytical and physical modelling. *Canadian Geotechnical Journal*, *57*(2), 236–245. https://doi.org/10.1139/cgj-2018-0622

Cui, K. F., Zhou, G. G., & Jing, L. (2021). Viscous effects on the particle size segregation in geophysical mass flows: Insights from immersed granular shear flow simulations. *Journal of Geophysical Research: Solid Earth*, *126*(8), e2021JB022274. https://doi.org/10.1029/2021JB022274

Cui, P., Zeng, C., & Lei, Y. (2015). Experimental analysis on the impact force of viscous debris flow. *Earth Surface Processes and Landforms*, *40*(12), 1644–1655. https://doi.org/10.1002/esp.3744

DeNatale, J. S., Iverson, R. M., Major, J. J., LaHusen, R. G., Fiegel, G. L., & Duffy, J. D. (1999). *Experimental testing of flexible barriers for containment of debris flows*. US Department of the Interior, US Geological Survey. https://doi.org/10.3133/OFR99205

Di Felice, R. (1994). The voidage function for fluid-particle interaction systems. *International Journal of Multiphase Flow*, *20*(1), 153–159. https://doi.org/10.1016/0301-9322(94)90011-6

Dugelas, L., Coulibaly, J. B., Bourrier, F., Lambert, S., Chanut, M. A., Olmedo, I., & Nicot, F. (2019). Assessment of the predictive capabilities of discrete element models for flexible rockfall barriers. *International Journal of Impact Engineering*, *133*, 103365. https://doi.org/10.1016/j.ijimpeng.2019.103365

Faug, T. (2015). Depth-averaged analytic solutions for free-surface granular flows impacting rigid walls down inclines. *Physical Review E*, *92*(6), 062310. https://doi.org/10.1103/PhysRevE.92.062310

Faug, T. (2021). Impact force of granular flows on walls normal to the bottom: Slow versus fast impact dynamics. *Canadian Geotechnical Journal*, *58*(1), 114–124. https://doi.org/10.1139/cgj-2019-0399

Faug, T., Beguin, R., & Chanut, B. (2009). Mean steady granular force on a wall overflowed by free-surface gravity-driven dense flows. *Physical Review E*, *80*(2), 021305. https://doi.org/10.1103/PhysRevE.80.021305

Faug, T., Caccamo, P., & Chanut, B. (2012). A scaling law for impact force of a granular avalanche flowing past a wall. *Geophysical Research Letters*, *39*(23), L23401. https://doi.org/10.1029/2012GL054112

Fávero Neto, A. H., Askarinejad, A., Springman, S. M., & Borja, R. I. (2020). Simulation of debris flow on an instrumented test slope using an updated Lagrangian continuum particle method. *Acta Geotechnica*, *15*(10), 2757–2777. https://doi.org/10.1007/s11440-020-00957-1

Fowler, H. J., Lenderink, G., Prein, A. F., Westra, S., Allan, R. P., Ban, N., et al. (2021). Anthropogenic intensification of short-duration rainfall extremes. *Nature Reviews Earth & Environment*, *2*(2), 107–122. https://doi.org/10.1038/s43017-020-00128-6

GEOVERT. (2016). GeoHazard mitigation: Shenandoah debris flow barrier. Retrieved from https://www.geovert.com/gedp-past-projects/Shenandoah/Debris-Flow-Barrier

Gong, S., Zhao, T., Zhao, J., Dai, F., & Zhou, G. G. (2021). Discrete element analysis of dry granular flow impact on slit dams. *Landslides*, *18*(3), 1143–1152. https://doi.org/10.1007/s10346-020-01531-2

Gori, T., Polimeni, A., Indolfi, C., Räber, L., Adriaenssens, T., & Münzel, T. (2019). Predictors of stent thrombosis and their implications for clinical practice. *Nature Reviews Cardiology*, *16*(4), 243–256. https://doi.org/10.1038/s41569-018-0118-5

Guerreiro, S. B., Fowler, H. J., Barbero, R., Westra, S., Lenderink, G., Blenkinsop, S., et al. (2018). Detection of continental-scale intensification of hourly rainfall extremes. *Nature Climate Change*, *8*(9), 803–807. https://doi.org/10.1038/s41558-018-0245-3

Heyman, J., Bohorquez, P., & Ancey, C. (2016). Entrainment, motion, and deposition of coarse particles transported by water over a sloping mobile bed. *Journal of Geophysical Research: Earth Surface*, *121*(10), 1931–1952. https://doi.org/10.1002/2015JF003672

Hirschberg, J., Fatichi, S., Bennett, G. L., McArdell, B. W., Peleg, N., Lane, S. N., et al. (2021). Climate change impacts on sediment yield and debris-flow activity in an alpine catchment. *Journal of Geophysical Research: Earth Surface*, *126*(1), e2020JF005739. https://doi.org/10.1029/2020JF005739

Hu, H., Zhou, G. G., Song, D., Cui, K. F. E., Huang, Y., Choi, C. E., & Chen, H. (2020). Effect of slit size on the impact load against debris-flow mitigation dams. *Engineering Geology*, *274*, 105764. https://doi.org/10.1016/j.enggeo.2020.105764

Huang, X., & Garcia, M. H. (1998). A Herschel–Bulkley model for mud flow down a slope. *Journal of Fluid Mechanics*, *374*, 305–333. https://doi.org/10.1017/S0022112098002845

Hübl, J., Suda, J., Proske, D., Kaitna, R., & Scheidl, C. (2009). Debris flow impact estimation. In *Proceedings of the 11th International Symposium on Water Management and Hydraulic Engineering, Ohrid, Macedonia* (Vol. 1, pp. 1–5).

Hungr, O., Morgan, G. C., & Kellerhals, R. (1984). Quantitative analysis of debris torrent hazards for design of remedial measures. *Canadian Geotechnical Journal*, *21*(4), 663–677. https://doi.org/10.1139/t84-073

Iverson, R. M. (1997). The physics of debris flows. *Reviews of Geophysics*, *35*(3), 245–296. https://doi.org/10.1029/97RG00426

Iverson, R. M., George, D. L., & Logan, M. (2016). Debris flow runup on vertical barriers and adverse slopes. *Journal of Geophysical Research: Earth Surface*, *121*(12), 2333–2357. https://doi.org/10.1002/2016JF003933

Iverson, R. M., Reid, M. E., Logan, M., LaHusen, R. G., Godt, J. W., & Griswold, J. P. (2011). Positive feedback and momentum growth during debris-flow entrainment of wet bed sediment. *Nature Geoscience*, *4*(2), 116–121. https://doi.org/10.1038/ngeo1040

Jiménez, J. M., & Davies, P. F. (2009). Hemodynamically driven stent strut design. *Annals of Biomedical Engineering*, *37*(8), 1483–1494. https://doi.org/10.1007/s10439-009-9719-9

Kloss, C., Goniva, C., Hager, A., Amberger, S., & Pirker, S. (2012). Models, algorithms and validation for opensource DEM and CFD–DEM. *Progress in Computational Fluid Dynamics, an International Journal*, *12*(2–3), 140–152. https://doi.org/10.1504/PCFD.2012.047457

Kong, Y., Guan, M. F., Li, X. Y., Zhao, J. D., & Yan, H. C. (2022). How flexible, slit and rigid barriers mitigate two-phase geophysical mass flows: A numerical appraisal (version 2) [Dataset]. Zenodo. https://doi.org/10.5281/zenodo.6577214

Kong, Y., Li, X., & Zhao, J. (2021). Quantifying the transition of impact mechanisms of geophysical flows against flexible barrier. *Engineering Geology*, *289*, 106188. https://doi.org/10.1016/j.enggeo.2021.106188

Kong, Y., Zhao, J., & Li, X. (2021). Hydrodynamic dead zone in multiphase geophysical flows impacting a rigid obstacle. *Powder Technology*, *386*, 335–349. https://doi.org/10.1016/j.powtec.2021.03.053

Kwan, J. S. H., & Cheung, R. W. M. (2012). *Suggestion on design approaches for flexible debris resisting barriers*. Discussion Note DN1/2012. Geotechnical Engineering Office, HKSAR.

Lambert, S., Toe, D., Mentani, A., & Bourrier, F. (2021). A meta-model-based procedure for quantifying the on-site efficiency of rockfall barriers. *Rock Mechanics and Rock Engineering*, *54*(2), 487–500. https://doi.org/10.1007/s00603-020-02298-7

Leonardi, A., Wittel, F. K., Mendoza, M., Vetter, R., & Herrmann, H. J. (2016). Particle–fluid–structure interaction for debris flow impact on flexible barriers. *Computer-Aided Civil and Infrastructure Engineering*, *31*(5), 323–333. https://doi.org/10.1111/mice.12165

Li, X., & Zhao, J. (2018). Dam-break of mixtures consisting of non-Newtonian liquids and granular particles. *Powder Technology*, *338*, 493–505. https://doi.org/10.1016/j.powtec.2018.07.021

Li, X., Zhao, J., & Kwan, J. S. (2020). Assessing debris flow impact on flexible ring net barrier: A coupled CFD-DEM study. *Computers and Geotechnics*, *128*, 103850. https://doi.org/10.1016/j.compgeo.2020.103850

Li, X., Zhao, J., & Soga, K. (2021). A new physically based impact model for debris flow. *Géotechnique*, *71*(8), 674–685. https://doi.org/10.1680/jgeot.18.P.365

Lichtenhan, C. (1973). Die Berechnung von Sperren in Beton und Eisenbeton, Kolloquium on Torrent Dams ODC 384.3 [In German]. In *Proc., Mitteilungen der Forstlichen Bundes-Versuchsanstalt* (pp. 91–127). Mitteilungender Forstlichen Bundensanstalt.

Liu, C., Yu, Z., & Zhao, S. (2020). Quantifying the impact of a debris avalanche against a flexible barrier by coupled DEM-FEM analyses. *Landslides*, *17*(1), 33–47. https://doi.org/10.1007/s10346-019-01267-8

Marchi, L., Comiti, F., Crema, S., & Cavalli, M. (2019). Channel control works and sediment connectivity in the European Alps. *Science of the Total Environment*, *668*, 389–399. https://doi.org/10.1016/j.scitotenv.2019.02.416

Ng, C. W. W., Liu, H., Choi, C. E., Kwan, J. S., & Pun, W. K. (2021). Impact dynamics of boulder-enriched debris flow on a rigid barrier. *Journal of Geotechnical and Geoenvironmental Engineering*, *147*(3), 04021004. https://doi.org/10.1061/(ASCE)GT.1943-5606.0002485

Ng, C. W. W., Song, D., Choi, C. E., Liu, L. H. D., Kwan, J. S. H., Koo, R. C. H., & Pun, W. K. (2017). Impact mechanisms of granular and viscous flows on rigid and flexible barriers. *Canadian Geotechnical Journal*, *54*(2), 188–206. https://doi.org/10.1139/cgj-2016-0128

Ng, C. W. W., Wang, C., Choi, C. E., De Silva, W. A. R. K., & Poudyal, S. (2020). Effects of barrier deformability on load reduction and energy dissipation of granular flow impact. *Computers and Geotechnics*, *121*, 103445. https://doi.org/10.1016/j.compgeo.2020.103445

Nicot, F., Gotteland, P., Bertrand, D., & Lambert, S. (2007). Multiscale approach to geo-composite cellular structures subjected to rock impacts. *International Journal for Numerical and Analytical Methods in Geomechanics*, *31*(13), 1477–1515. https://doi.org/10.1002/nag.604

Potyondy, D. O., & Cundall, P. A. (2004). A bonded-particle model for rock. *International Journal of Rock Mechanics and Mining Sciences*, *41*(8), 1329–1364. https://doi.org/10.1016/j.ijrmms.2004.09.011

Pudasaini, S. P., & Mergili, M. (2019). A multi-phase mass flow model. *Journal of Geophysical Research: Earth Surface*, *124*(12), 2920–2942. https://doi.org/10.1029/2019JF005204

Remaître, A., Malet, J. P., Maquaire, O., Ancey, C., & Locat, J. (2005). Flow behaviour and runout modelling of a complex debris flow in a clay-shale basin. *Earth Surface Processes and Landforms: The Journal of the British Geomorphological Research Group*, *30*(4), 479–488. https://doi.org/10.1002/esp.1162

Scheidl, C., Chiari, M., Kaitna, R., Müllegger, M., Krawtschuk, A., Zimmermann, T., & Proske, D. (2013). Analysing debris-flow impact models, based on a small scale modelling approach. *Surveys in Geophysics*, *34*(1), 121–140. https://doi.org/10.1007/s10712-012-9199-6

Shan, T., & Zhao, J. (2014). A coupled CFD-DEM analysis of granular flow impacting on a water reservoir. *Acta Mechanica*, *225*(8), 2449–2470. https://doi.org/10.1007/s00707-014-1119-z

Smuts, E. M., Deglon, D. A., & Meyer, C. J. (2012). Methodology for CFD-DEM modelling of particulate suspension rheology. In *Proceedings of the Ninth International Conference on CFD in the Minerals and Process Industries CSIRO, Melbourne, Australia* (pp. 37–53).

Song, D., Chen, X., Zhou, G. G., Lu, X., Cheng, G., & Chen, Q. (2021). Impact dynamics of debris flow against rigid obstacle in laboratory experiments. *Engineering Geology*, *291*, 106211. https://doi.org/10.1016/j.enggeo.2021.106211

Song, D., Choi, C. E., Ng, C. W. W., Zhou, G. G., Kwan, J. S., Sze, H. Y., & Zheng, Y. (2019). Load-attenuation mechanisms of flexible barrier subjected to bouldery debris flow impact. *Landslides*, *16*(12), 2321–2334. https://doi.org/10.1007/s10346-019-01243-2

Song, D., Choi, C. E., Ng, C. W. W., & Zhou, G. G. D. (2018). Geophysical flows impacting a flexible barrier: Effects of solid-fluid interaction. *Landslides*, *15*(1), 99–110. https://doi.org/10.1007/s10346-017-0856-1

Song, D., Choi, C. E., Zhou, G. G. D., Kwan, J. S., & Sze, H. Y. (2018). Impulse load characteristics of bouldery debris flow impact. *Géotechnique Letters*, *8*(2), 111–117. https://doi.org/10.1680/jgele.17.00159

Song, D., Ng, C. W. W., Choi, C. E., Zhou, G. G., Kwan, J. S., & Koo, R. C. H. (2017). Influence of debris flow solid fraction on rigid barrier impact. *Canadian Geotechnical Journal*, *54*(10), 1421–1434. https://doi.org/10.1139/cgj-2016-0502

Song, D., Zhou, G. G., Chen, X. Q., Li, J., Wang, A., Peng, P., & Xue, K. X. (2021). General equations for landslide-debris impact and their application to debris-flow flexible barrier. *Engineering Geology*, *288*, 106154. https://doi.org/10.1016/j.enggeo.2021.106154

Sun, P. N., Le Touzé, D., Oger, G., & Zhang, A. M. (2021). An accurate FSI-SPH modeling of challenging fluid-structure interaction problems in two and three dimensions. *Ocean Engineering*, *221*, 108552. https://doi.org/10.1016/j.oceaneng.2020.108552

Tan, D. Y., Yin, J. H., Feng, W. Q., Zhu, Z. H., Qin, J. Q., & Chen, W. B. (2019). New simple method for calculating impact force on flexible barrier considering partial muddy debris flow passing through. *Journal of Geotechnical and Geoenvironmental Engineering*, *145*(9), 04019051. https://doi.org/10.1061/(ASCE)GT.1943-5606.0002133

Tiberghien, D., Laigle, D., Naaim, M., Thibert, E., & Ousset, F. (2007). Experimental investigations of interaction between mudflow and an obstacle. In *Debris-flow hazards mitigation: Mechanics, prediction and assessment* (pp. 681–687). MillPress.

Vagnon, F. (2020). Design of active debris flow mitigation measures: A comprehensive analysis of existing impact models. *Landslides*, *17*(2), 313–333. https://doi.org/10.1007/s10346-019-01278-5

Vicari, H., Ng, C. W., Nordal, S., Thakur, V., De Silva, W. R. K., Liu, H., & Choi, C. E. (2021). The effects of upstream flexible barrier on the debris flow entrainment and impact dynamics on a terminal barrier. *Canadian Geotechnical Journal*, *59*(6), 1007–1019. https://doi.org/10.1139/cgj-2021-0119

Von Boetticher, A., Turowski, J. M., McArdell, B. W., Rickenmann, D., & Kirchner, J. W. (2016). DebrisInterMixing-2.3: A finite volume solver for three-dimensional debris-flow simulations with two calibration parameters – Part 1: Model description. *Geoscientific Model Development*, *9*(9), 2909–2923. https://doi.org/10.5194/gmd-9-2909-2016

Von Boetticher, A., Volkwein, A., Wüchner, R., Bletzinger, K. U., & Wendeler, C. (2011). Numerical modeling of shallow landslide impacts on flexible protection systems and its validation with full scale testing. In *COUPLED IV: Proceedings of the IV International Conference on Computational Methods for Coupled Problems in Science and Engineering* (pp. 731–742). CIMNE. Retrieved from http://hdl.handle.net/2117/327389

Wendeler, C. (2016). Debris-flow protection systems for mountain torrents. *WSL Berichte*. Swiss Federal Institute for Forest, Snow and Landscape Research WSL.

Wendeler, C., & Volkwein, A. (2015). Laboratory tests for the optimization of mesh size for flexible debris-flow barriers. *Natural Hazards and Earth System Sciences*, *15*(12), 2597–2604. https://doi.org/10.5194/nhess-15-2597-2015

Wendeler, C., Volkwein, A., McArdell, B. W., & Bartelt, P. (2019). Load model for designing flexible steel barriers for debris flow mitigation. *Canadian Geotechnical Journal*, *56*(6), 893–910. https://doi.org/10.1139/cgj-2016-0157

Wu, K., Yang, D., Wright, N., & Khan, A. (2018). An integrated particle model for fluid–particle–structure interaction problems with free-surface flow and structural failure. *Journal of Fluids and Structures*, *76*, 166–184. https://doi.org/10.1016/j.jfluidstructs.2017.09.011

Xu, H., Gentilini, C., Yu, Z., Qi, X., & Zhao, S. (2018). An energy allocation based design approach for flexible rockfall protection barriers. *Engineering Structures*, *173*, 831–852. https://doi.org/10.1016/j.engstruct.2018.07.018

Zhang, Z., Walter, F., McArdell, B. W., Wenner, M., Chmiel, M., de Haas, T., & He, S. (2021). Insights from the particle impact model into the high-frequency seismic signature of debris flows. *Geophysical Research Letters*, *48*(1), e2020GL088994. https://doi.org/10.1029/2020GL088994

Zhao, J., & Shan, T. (2013). Coupled CFD-DEM simulation of fluid-particle interaction in geomechanics. *Powder Technology*, *239*, 248–258. https://doi.org/10.1016/j.powtec.2013.02.003

Zhao, L., He, J. W., Yu, Z. X., Liu, Y. P., Zhou, Z. H., & Chan, S. L. (2020). Coupled numerical simulation of a flexible barrier impacted by debris flow with boulders in front. *Landslides*, *17*(12), 2723–2736. https://doi.org/10.1007/s10346-020-01463-x

Zhou, G. G., Cui, K. F., Jing, L., Zhao, T., Song, D., & Huang, Y. (2020). Particle size segregation in granular mass flows with different ambient fluids. *Journal of Geophysical Research: Solid Earth*, *125*(10), e2020JB019536. https://doi.org/10.1029/2020JB019536

Zhou, G. G., Du, J., Song, D., Choi, C. E., Hu, H. S., & Jiang, C. (2020). Numerical study of granular debris flow run-up against slit dams by discrete element method. *Landslides*, *17*(3), 585–595. https://doi.org/10.1007/s10346-019-01287-4

Zhou, Z. Y., Kuang, S. B., Chu, K. W., & Yu, A. B. (2010). Discrete particle simulation of particle-fluid flow: Model formulations and their applicability. *Journal of Fluid Mechanics*, *661*, 482–510. https://doi.org/10.1017/S002211201000306X

Zhu, Z. H., Yin, J. H., Qin, J. Q., & Tan, D. Y. (2019). A new discrete element model for simulating a flexible ring net barrier under rockfall impact comparing with large-scale physical model test data. *Computers and Geotechnics*, *116*, 103208. https://doi.org/10.1016/j.compgeo.2019.103208

References From the Supporting Information

Faug, T. (2015). Macroscopic force experienced by extended objects in granular flows over a very broad Froude-number range. *The European Physical Journal E*, *38*(5), 1–10. https://doi.org/10.1140/epje/i2015-15034-3

Geobrugg, A. G. (2012). Geobrugg: Barreras contra flujos de detritus. Retrieved from https://www.youtube.com/watch?v=hMu9VAEGe1A

Iverson, R. M., & Denlinger, R. P. (2001). Flow of variably fluidized granular masses across three-dimensional terrain: 1. Coulomb mixture theory. *Journal of Geophysical Research*, *106*(B1), 537–552. https://doi.org/10.1029/2000JB900329

Kafui, K. D., Thornton, C., & Adams, M. J. (2002). Discrete particle-continuum fluid modelling of gas–solid fluidised beds. *Chemical Engineering Science*, *57*(13), 2395–2410. https://doi.org/10.1016/S0009-2509(02)00140-9

Logan, M., Iverson, R. M., & Obryk, M. K. (2018). Video documentation of experiments at the USGS debris-flow flume 1992–2018. USGS open-file report. Retrieved from http://pubs.usgs.gov/of/2007/1315/

Silbert, L. E., Ertaş, D., Grest, G. S., Halsey, T. C., Levine, D., & Plimpton, S. J. (2001). Granular flow down an inclined plane: Bagnold scaling and rheology. *Physical Review E*, *64*(5), 051302. https://doi.org/10.1103/PhysRevE.64.051302